Daniel Matté

Molecular dynamics simulations of the isotopic effect on nanoscale friction

Caxias do Sul - RS, Brazil

2021

Daniel Matté

Molecular dynamics simulations of the isotopic effect on nanoscale friction

Work supervised by Cláudio Antônio Perottoni and Carlos Alejandro Figueroa, presented to the Graduate Program in Engineering and Materials Science of the University of Caxias do Sul as a partial requirement for obtaining the Master degree in Engineering and Materials Science.

University of Caxias do Sul – UCS

Graduate Program in Engineering and Materials Science

Supervisor: Cláudio Antônio Perottoni

Co-supervisor: Carlos Alejandro Figueroa

Caxias do Sul - RS, Brazil

2021

Daniel Matté

Molecular dynamics simulations of the isotopic effect on nanoscale friction

Work supervised by Cláudio Antônio Perottoni and Carlos Alejandro Figueroa, presented to the Graduate Program in Engineering and Materials Science of the University of Caxias do Sul as a partial requirement for obtaining the Master degree in Engineering and Materials Science.

Approved work. Caxias do Sul - RS, Brazil, February 18th, 2021:

Cláudio Antônio Perottoni
Supervisor

Carlos Alejandro Figueroa
Co-supervisor

Alexandre Fassini Michels

André Rodrigues Muniz

María Cristina Moré Farias

Caxias do Sul - RS, Brazil
2021

To my mother Lorilde (in memoriam), who is present every day of my life, and wherever she is, I am sure she will look after me. To my father Gilberto, who managed to keep the family together in difficult times and is an example for me.

Acknowledgements

Resumo

As simulações computacionais estão se tornando cada vez mais úteis para o estudo do atrito, permitindo a aplicação de condições controladas, desacoplamento de mecanismos e configurações que geralmente não são alcançáveis em experimentos físicos, garantindo que nenhuma outra variável indesejável esteja agindo no sistema. Neste trabalho, simulações de dinâmica molecular (MD) foram usadas para explorar sistematicamente o efeito de massa do isótopo na contribuição fonônica para o atrito, simulando diferentes condições de carga, direção de deslizamento e cobertura de superfície para superfícies planas de cristal único de diamante [111] passivadas com H. Simulações foram realizadas utilizando o potencial Adaptive Intermolecular Reactive Empirical Bond-Order (AIREBO), incluindo as interações de van der Waals. O coeficiente de atrito foi considerado independente da massa atômica do adsorbato para ambas as direções de deslizamento simuladas. Além disso, pelo menos nas condições simuladas, uma simples redução na cobertura da superfície também não afetou significativamente o coeficiente de atrito. Um aumento acentuado da força de atrito foi observado apenas quando a camada de passivação foi modificada pela introdução de defeitos altamente reativos. Por conseguinte, os resultados das simulações de dinâmica molecular dão suporte a um efeito isotópico indireto no atrito, mas apenas na medida em que os defeitos criados na camada de passivação levam à formação de superfícies altamente reativas.

Palavras-chave: atrito fonônico. efeito isotópico. simulação de dinâmica molecular.

Abstract

Computer simulations are becoming increasingly useful for studying friction, enabling the application of controlled conditions, uncoupling mechanisms, and set-ups that are not usually achievable in physical experiments, ensuring that no other undesirable variable is acting on the system. In this work, molecular dynamics (MD) simulations were used to systematically explore the isotope's mass effect on the phononic contribution to friction by simulating different load conditions, sliding direction, and surface coverage of H-passivated flat [111] single-crystal diamond surfaces. Simulations were performed using the Adaptive Intermolecular Reactive Empirical Bond-Order (AIREBO) potential, including van der Waals interactions. The coefficient of friction was found to be independent of the adsorbate atomic mass for both sliding directions simulated. Furthermore, at least in the simulated conditions, a simple reduction in surface coverage also did not significantly affect the coefficient of friction. A marked increase of friction force was observed only when the passivation layer was modified by introducing highly reactive defects. Accordingly, the results from MD simulations give support to an indirect isotopic effect on friction, but only to the extent that defects created in the passivation layer lead to the formation of highly reactive surfaces.

Keywords: phononic friction. isotopic effect. MD simulation.

List of Figures

List of abbreviations and acronyms

2D	Two-dimensional
AFM	Atomic Force Microscopy
AIC	Akaike Information Criterion
AIREBO	Adaptive Intermolecular Reactive Empirical Bond-Order
CESUP	Centro Nacional de Supercomputação
COMB	Charge-Optimized Many Body
CPU	Central Processing Unit
EAM	Embedded Atom Method
EDIP	Environment Dependent Interaction Potential
FCC	Face-Centered Cubic
GNU	Gnu's Not Unix
HT	Hyper-Threading
LAMMPS	Large-scale Atomic/Molecular Massively Parallel Simulator
LCBOP	Long-range Carbon Bond-Order Potential
LJ	Lennard-Jones Potential
MD	Molecular Dynamics
NACAD	Núcleo Avançado de Computação de Alto Desempenho
NPT	Isothermal-Isobaric ensemble
NVE	Microcanonical ensemble
NVT	Canonical ensemble
OVITO	Open Visualization Tool
PBC	Periodic Boundary Conditions
QCM	Quartz Crystal Microbalance

RAM	Random Access Memory
ReaxFF	Reactive ForceField
REBO	Reactive Empirical Bond-Order
TRAVIS	Trajectory Analyzer and Visualizer
US	United States

List of symbols

%	Percentage
H	Hydrogen
D	Deuterium
m	Atomic/molecular mass and meter (when used as a unit)
μ_r	Reduced mass of the system
m_s	Mass of the substrate atoms
u	Unified atomic mass unit
F	Force
μ	Coefficient of friction
L	Applied load
F_s	Static friction force
F_k	Kinetic friction force
ms	Millisecond
F_{ext}	Externally applied force
F_{adh}	Force of adhesion
F_{adh}	Adhesive component of friction
A_r	Real area of contact
s^s	Stress needed to start or to maintain sliding
Δ	Delta (prefix to indicate a finite difference in the variable)
M	Distance
a	One atomic dimension
θ	Average angle
ε	Small fraction of the total energy of adhesion

γ	Surface energy of the material
P	Pressure
s_0^s	Critical shear stress
α_P	Proportionality constant
v	Sliding velocity
η_m	Sliding interface's viscosity
U_0	Periodic potential
η_{subs}	Non-phononic energy dissipation
c	Temperature and lattice spacing dependent constant
t_{slip}	Slip time
e	Euler's number
τ	Tangential stress
A	Contact area
δA	The area occupied per the lubrication molecule
U	Periodically corrugated adsorbate-substrate potential
u_p	Partial corrugated adsorbate-substrate potential
$\sum$	Sum
i	Particle i
r	Coordinate of a random adsorbate or particle
V^P	Adsorbate-adsorbate potential
j	Particle j
v_p	Partial adsorbate-adsorbate interaction potential
$\langle...\rangle$	Thermal average
N_1	Number of adsorbates in the first layer in direct contact with the substrate
$\bar{\eta}$	Sliding friction

$\cdot$	First derivative ((Newton's notation)
N	Total number of adsorbates and number of particles
P_1	Ratio between N_1 and N
∂	Partial derivative
t	Time
$\ddot{}$	Second derivative (Newton's notation)
f	Stochastic fluctuation force
η	Friction
α	Index α in the fluctuation-dissipation theorem
β	Index β in the fluctuation-dissipation theorem
k_B	Boltzmann constant
T	Temperature
E_B	Adsorbate binding energy
z	z-axis perpendicular to the surface
cos	Cosine
x	x-axis (forming a plane with y-axis)
y	y-axis
k	Wave vector
π	Pi number
q	Coordinate of the perpendicular vibrational mode
$\omega_\perp$	Vibrational resonance frequency of the vertical vibration
$\omega_\parallel$	Vibrational resonance frequency of the parallel vibration
$\int$	Integration
$'$	First derivative (Lagrange's notation)
$''$	Second derivative (Lagrange's notation)
∞	Infinite

ω_c	Maximum phonon frequency of the solid
$\eta_\perp$	Perpendicular friction
$\eta_\parallel$	Parallel friction
ρ	Mass density
c_T	Substrate transverse sound velocity
$\hbar$	Reduced Planck constant
ω	Vibrational resonance frequency
ω_0	Adsorbate vibrational resonance frequency
λ	Wavelength of the emitted phonons
c_L	Substrate perpendicular sound velocity
n_a	Number of adsorbates per unit area
E	Energy
τ_c	Collision time
$\sim$	Approximately
$\propto$	Proportionality
V	Volume
ν	Frequency
C	Carbon
∇	Gradient of a function
V^{LJ}	Lennard-Jones potential
ϵ	Energy well depth
σ_D	Constant that represents the distance where the interatomic potential is zero
Å	Ångström
E^{AIREBO}	AIREBO resultant interaction (energy)
E^{REBO}	REBO energy

E^{LJ}	Lennard-Jones energy
E^{tors}	Torsion energy
V^R	Repulsive pairwise potential
V^A	Attractive pairwise potential
b	Many-body term
$b*$	Many-body term in the nonbonded portions of the AIREBO potential
S	Universal switching function
V^{tors}	Torsional potential
t_r	Scaling function t_r on the AIREBO potential
t_b	Scaling function t_b on the AIREBO potential
C^S	Connectivity switch
w	Dihedral angle
k	Particle k
l	Particle l
E_K	Kinetic energy
E_P	Potential energy
f_D	Kinetic degrees of freedom
ξ	Dynamic variable in the Nosé-Hoover thermostat
g	Grams
mol	Unit of amount of substance (mole)
ps	Picosecond
K	Kelvin unit
k_m	Spring force constant
eV	Electronvolt
$\circ$	Degree
meV	Millielectronvolt

fs	Femtosecond
GB	Gigabyte
GHz	Gigahertz
TFlop	Teraflop
cm	Centimeter
nN	Nanonewton
nm	Nanometer
s	Second
µm	Micrometer
GPa	Gigapascal
σ	Standard deviation

Contents

Introduction

Understanding the mechanisms involved in the dissipation of energy due to friction is a fundamental step in developing new technologies for industrial processes that are more energetically efficient, with longer lifespan, and more competitive [1, 2]. The control of friction is also key to increase the reliability of micro- and nano-scale systems, as wear is known to be a barrier to practical use of these systems in various technologies due to the relatively high surface forces usually present in these situations [3].

The scientific investigation of friction initiated with Leonardo da Vinci, who described in his notebooks the proportionality of friction force on the applied load [4]. In 1699, Guillaume Amontons rediscovered this relation (Amontons' Laws of Friction), later complemented by Coulomb's works [5]. These classical laws of friction were empirically derived based on macroscopic observations. Nowadays, the micro- and nanoscopic origin of friction has become the focus of much scientific interest [6, 7].

Experiments on friction at the nanoscale can be performed using a variety of techniques [6, 8]. Atomic force microscopy (AFM), in particular, has been widely used in studies of nanoscale friction of various systems [9–11]. Friction force at the nanoscale can be heavily influenced by physical and chemical characteristics of the surfaces in contact. Indeed, several distinct mechanisms can be involved in the energy dissipation from sliding surfaces [12]. However, in experimental situations, it is not always possible to evaluate and separate these different contributions where dissipation mechanisms may be coupled. Therefore, computer simulations emerge as an option to explore the relative importance of different contributions to friction forces. In molecular dynamics (MD) simulations, it is possible to impose well-controlled conditions that are not easily achievable by experimental conditions and, at the same time, ensure that there are no other undesirable variables influencing the system's response. For this reason, MD studies have become increasingly used to understand the fundamental mechanisms of surface interaction at the nanoscale and as an aid to interpret experimental observations [13–15].

Several techniques are available to modify the friction force between sliding surfaces. The chemical passivation of surfaces, with hydrogen (H), for example, has been shown to be an effective method to reduce friction and adhesion [16]. Formally, it is adequate to distinguish between *static* and *kinetic* friction. In the latter, the opposing force to motion is dependent on a viscous damping factor. Phonon excitation is one of the contributions to the viscous damping and energy dissipation by phonon creation and has been studied both analytically and by MD simulations [6]. Based on this premise and in order to explore experimentally the phononic contribution to friction, Cannara et al. [9] showed

that friction was reduced by about 20 % when a diamond surface was passivated with deuterium (D) – a H isotope – compared to a H-passivated surface. This isotopic effect on friction was interpreted in terms of a modified Persson's model [17, 18], according to which, increasing the mass of adsorbates (while keeping the chemical nature unaltered) reduce friction because lighter specimens collide more frequently, thus increasing energy dissipation [9]. In a nutshell, keeping all the same except for the mass of the chemisorbed passivation atoms, the energy-transfer model of Cannara et al. yields a friction force that scales as m/μ_r^2, where m is the atomic mass of the adsorbate and $\mu_r = m\,m_s/(m+m_s)$ is the reduced mass (m_s is the mass of the substrate atoms, e.g., carbon in a diamond surface). For a deuterium-passivated diamond surface, the model suggests a 40 % reduction of friction force as compared to the H-passivated surface, more than enough to account for the observed effect.

However, despite the robust experimental evidences of an isotopic effect on nanoscale friction, the precise mechanism behind this phenomenon is still a motive of controversy. In fact, it has been pointed out that, despite the increased collision frequency for lighter atoms, the smaller momentum transfer in each collision should render this mass effect ineffective in reducing friction, as pointed out by Mo et al. [19]. Indeed, in their MD study, Mo et al. simulated the sliding of a diamond tip on a diamond surface, both surfaces passivated by hydrogen atoms. In their computer simulations, the mass of the H atoms varied from 1 to 7 u (unified atomic mass units), without any noticeable effect on friction. In those simulations, the van der Waals interactions were not included in the interatomic potential to reduce the computational cost. Mo et al. [19] thus proposed that the effect observed by Cannara et al. can be explained by small differences, around 2 %, in surface coverage, which depends on the relative thermal stability of H- and D- passivated surfaces. However, despite this hypothesis being supported by comparing results obtained for 100 % and 80 % passivated surfaces, no MD simulation was performed for the low concentration of surface defects suggested as a possible explanation for the isotopic effect reported by Cannara et al.

In this work, a comprehensive set of molecular dynamics simulations were performed aiming to explore the effect of the adsorbate mass and coverage factor on the friction between two passivated diamond surfaces. Simulations were performed in different conditions of normal load, sliding direction and surface coverage, extending previous analysis and allowing to probe the premises described in the preceding paragraphs. The MD simulations were carried out with the specific purpose of exploring the possible effect of the atomic mass of atoms in the passivation layer and, also, the creation of defects in this passivation layer on the friction between passivated diamond surfaces.

This document is divided into three parts. The theoretical basis of the friction phenomena and the molecular dynamics simulations theory are presented in the first part.

The adopted methodology is described with emphasis in the developed scripts' main points (the entire scripts are available in the Appendix section). The description of the results and the discussions based on them are shown in the second part of the work. Finally, the conclusions are presented in the third part of this work.

Part I

Theoretical Basis

1 Theoretical Basis

1.1 Historical overview

Friction is part of human history, and its effects were used to chip stones to have tools or start a fire by rubbing pieces of wood. Some Egyptian paintings already illustrated systems done for moving significant parts used in their constructions. Even with humanity making use of many effects of the friction, its study only was documented by Leonardo da Vinci (1452-1519). Figure 1 shows the experiment made by Leonardo da Vinci, a block of wood is attached to another object through a cord which is over a fixed cylinder, free to rotate (there was the possibility of changing the weight of the second object) [20].

Figure 1 – Drawing from da Vinci's notebook (Source: Codex Arundel, British Library, London (Arundel folio 41r).
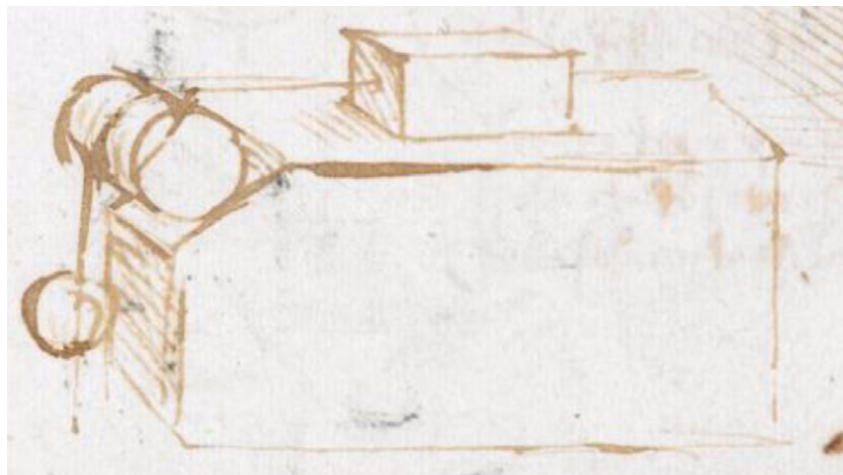
Based on tests with inclined planes and variations on the apparent area, the following remarks were found in his records [4, 20]:

- The friction force between two sliding surfaces is proportional applied load used to press the surfaces;

- The friction force has no dependence on the apparent contact area between the surfaces.

It was not recognized back then, but in 1699 Guillaume Amontons rediscovered these relations, and they became known as Amonton's laws of friction. The first postulate

is a linear equation

$$F = \mu L, \tag{1.1}$$

where μ is the coefficient of friction, F is the friction force, and L is the applied load [4]. Equation 1.1 also implies that friction is independent of the apparent contact area (second law) [6].

1.2 Macroscopic considerations

1.2.1 The three laws of friction

As described in the Historical overview section, the two laws of friction attributed to Amontons give us two principal affirmations: the friction force is proportional to the normal load and is independent of the apparent area of contact. These are empirical rules, and some exceptions exist without infringing fundamental laws of nature [21]. About the second affirmation, it is currently known that friction increases with the real contact area, which generally increases with load. The third law of friction provided by Coulomb (1736–1806) suggests that the kinetic friction is independent of sliding velocity. This affirmation is not always accurate, but in general, the coefficient of friction has a slight negative slope as a function of sliding velocity, and this approach can be considered acceptable. It is essential to highlight that a slight change in the sliding velocity in some situations results in a more significant reduction in the coefficient of friction [6, 21].

1.2.2 Static friction and steady sliding

Suppose a block with an attached spring pulled in a constant velocity with no changes in normal force. At the beginning of the process, the block continues at rest until the maximum static friction force is achieved. Usually, we think of static friction as a constant value, but in fact, the friction force increments linearly at the same time as the spring is being loaded. This behavior can be visualized in Figure 2, where the friction force increases at a maximum value followed by a small decrease and a steady sliding motion [6, 22].

1.2.3 Stick-slip

In our daily lives, we face some sounds that cause us discomfort, for example, the creaking of a door and the squeaks of nails in a blackboard. However, on other occasions, for example, when listening to a violin, the tone becomes music for our mind. These situations described are manifestations of the same phenomenon known as stick-slip. During the

Figure 2 – Friction force as a function of time or displacement; F_s is the static friction force required to commence the sliding, and F_k is the kinetic friction force required to keep moving [22].
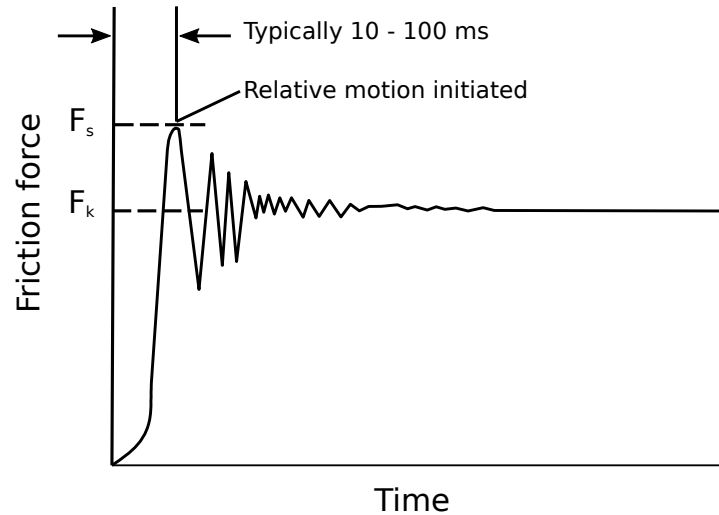
stick-slip, friction has the behavior described in Figure 3, with successive stops during the motion, followed by a slip. This nature is a consequence of the static friction having a higher value than the kinetic friction, plus the fact that the kinetic friction decreases with the increase of the sliding speed (remember that the third law of friction is just a good approximation) [6]. For an atomistic explanation for the stick-slip phenomena, refer to the subsection 1.3.2.

Figure 3 – Friction force as a function of time or distance showing stick-slip phenomenon [22].
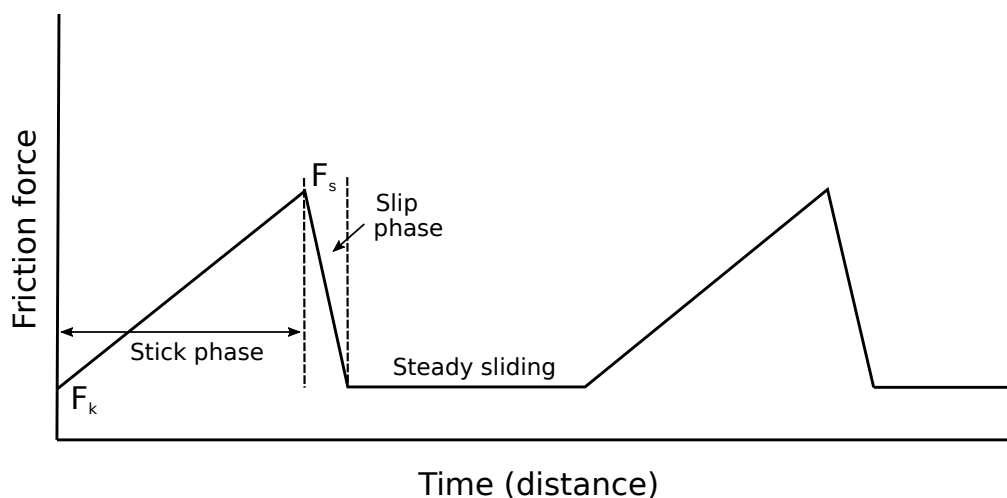
Suppose the same block described before, during the stick-slip; the block stays in rest until the static friction force is achieved, then the movement starts. Faster in the beginning, but decreasing the velocity after passing the spring's equilibrium position, until

the point, it stops suddenly. What determines if the motion will have a steady nature or a stick-slip nature is the combination of the spring's pull velocity and the spring stiffness (if these values are sufficiently high, the steady motion will occur) [6, 22].

1.3 Atomistic origins of friction

When analyzing at the atomic level, the two main contributors to friction force can be deeply interpreted as the *adhesion* term, defined as the resistance to sliding originated from the interactions forces between atoms on opposite surfaces, and the *plowing* term, defined as the resistance to sliding, originated from the work of asperities of the most robust surface plastically deforming the smooth surface [6]. In this work, the elastic deformation is the object of study.

1.3.1 Adhesive friction

The contribution of adhesion to friction can be expressed through a modified version of Amontons's equation (Equation 1.1),

$$F = \mu(F_{ext} + F_{adh}), \tag{1.2}$$

where F_{ext} is the externally applied load and F_{adh} is the adhesive contribution to the loading force [6]. Bowden and Tabor [23] proposed that the adhesive component of friction F_{adh} is proportional to the real area of contact:

$$F_{adh} = A_r s, \tag{1.3}$$

where s is the stress needed to start or to maintain sliding (s is the shear strength caused by the interaction forces between the sliding atoms), A_r is the real area of contact. The friction is proportional to the normal force because the real area of contact is proportional to load (valid for both plastic or elastic deformation of the contacting asperities) [6].

1.3.1.1 A simple model for adhesive friction

To initiate the understanding of the adhesive friction at the atomic level, a very simple model known as the cobblestone model [24, 25], see Figure 4, in analogy to the lateral force needed to overcome the cobblestones and start the movement of a cart, will be taken. To commence sliding, a small distance ΔM must exist between the surfaces, allowing the atoms on the opposing surfaces to have enough range to slide over each other. After a laterally sliding of about one atomic dimension a, the atoms experience the next minimum energy bonding site.

Figure 4 – Cobblestone model sketch of friction based on purely geometric considerations of the average angle θ by which the atomic asperity has to move upward against the normal load before it can slides. One atomic dimension is represented by a. Adapted from BERMAN (2018) [26].
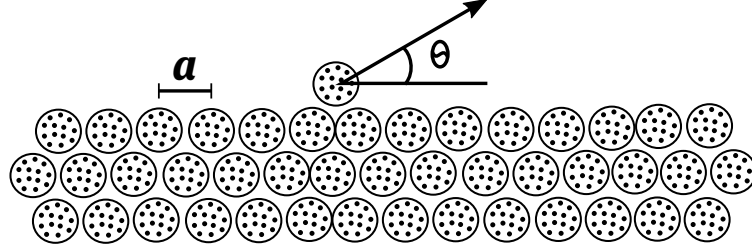
Assuming that the external force is negligible compared to the internal interatomic force caused by the adhesive interactions among atoms and that all energy is dissipated as heat, the following relationship can be described [6]:

$$a \times F_{adh} = \Delta M \times F_{adh} = \varepsilon(2\gamma A_r), \tag{1.4}$$

where F_{adh} is the total force of adhesion, $\Delta M \times F_{adh}$ is the energy required to separate both surfaces and start sliding, ε is a small fraction of the total energy of adhesion $2\gamma A_r$, where γ is the surface energy of the material. Thus, the shear strength expression can be written as:

$$s^s = \frac{F_{adh}}{A_r} = \frac{2\gamma\varepsilon}{a}. \tag{1.5}$$

In some cases, the shear strength s^s increases linearly with the contact pressure P. Dividing the Equation 1.2 per the real area of contact A_r, results in:

$$s^s = s_0^s + \alpha_P P. \tag{1.6}$$

where s_0^s is the critical shear stress needed to initiate motion and α_P is a proportionality constant [27]. When the interactions between the sliding surfaces are weak, the external contact pressure is comparable to the internal pressure, a remarkable linear dependence of the shear strength is observed. In these cases, even with a constant real area of contact, Amonton's law appears to remain valid [28, 29].

1.3.2   The Prandtl-Tomlinson model

As an overview, we chose the simple Prandtl-Tomlinson model to exemplify the static friction at an atomic level. This model consists of sliding atoms connected by springs to a rigid part, over a periodical potential, as shown in Figure 5 for the one-dimension

case. In the beginning, the system is at rest. Then, the slider initiates the motion, and the system shows static friction until the potential barriers are overcome by the elastic spring stress. When this occurs, the individual atoms slip to their next stable position. During the slips, the elastic energy stored is released in the form of kinetic energy, dissipated as heat. If the potential barrier height is lower than the starting point for slips to occur, the atoms will move smoothly over the periodic potential [6].

Figure 5 – One-dimensional Prandtl-Tomlinson model where the atoms are connected to a slider by overdamped springs, experiencing a periodic potential as they slide over a substrate surface [6].
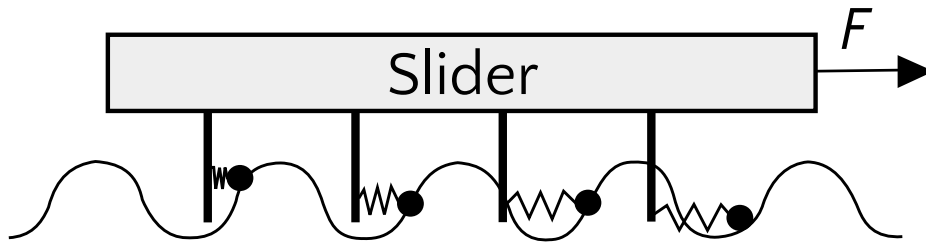
1.3.3 Atomistic models for kinetic friction

It is usual to separate the origin of the friction at the atomic level into two regimes: *static friction*, that is, the force needed to beat the potential energy barriers between atoms, starting the sliding; *kinetic friction*, that is, the dissipative energy mechanisms when atoms slide over each other [6]. Considering a sufficiently smooth surface, where an activation barrier is small, a little force is needed to start the sliding. It can be assumed that the force F contrary to motion is purely viscous,

$$F = m\eta_m v, \tag{1.7}$$

where m is the molecular mass, v is the sliding velocity, and η_m represents the sliding interface's viscosity. In most cases, the phonon excitations (sliding-induced atomic vibrations) are the primary source of the viscous damping, and lastly, these excitations are transformed into heat. A periodic potential with corrugation U_0 has been used in analytical models for adsorbed noble gases sliding on surfaces for describing the adatom-substrate interaction. The following relation describes η_m:

$$\eta_m = \eta_{subs} + cU_0^2, \tag{1.8}$$

where η_{subs} is the non-phononic energy dissipation, such as electronic excitations, c is a temperature and lattice spacing dependent constant. Here we can consider again that

during sliding, the adsorbed layers experience only viscous friction (Equation 1.7) and can be modeled by a slip time,

$$t_{slip} = \frac{1}{\eta_m},$$ (1.9)

where t_{slip} is inversely proportional to η_m and is defined as the time for the velocity of the adsorbed layer to decay by $1/e$, subsequently to remove the driving force F [6].

1.3.4 Sliding of adsorbate layers

Let us consider an elastic block on a substrate with a monolayer of lubrication molecules between them and an external force F_{ext} applied on the block parallel to the substrate (see Figure 6 left). Considering a stationary case, the F_{ext} must act on the lubrication layer too. The tangential stress exerted by the block on the lubrication layer is [17]:

$$\tau = \frac{F_{ext}}{A},$$ (1.10)

where A is the contact area between the block and the substrate. The absolute tangential force exerted by the block on a particular lubrication molecule will oscillate in time but has the average value $\tau \delta A$, where δA is the area occupied per the lubrication molecule. For the average treatment, we can remove the block assuming that the force $F = \sigma \delta A$ operates on each adsorbate (see Figure 6 right), being a good approximation for homogeneous lubrication layers [17].

Figure 6 – An external force F_{ext} acts on the block parallel to the substrate, and the elastic block slides on a substrate with a lubrication molecules monolayer represented by black dots (left). In a mean-field approximation, the block's response on the lubrication layer is substituted by uniform tangential stress $\tau = F_{ext}/A$ acting on the adsorbed monolayer (right). Adapted from PERSSON (2000) [17].
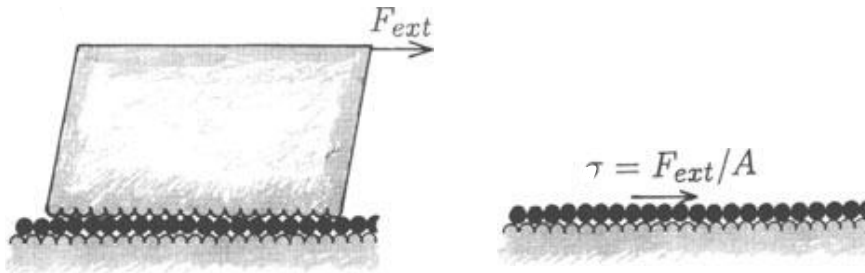
1.3.4.1 The Brownian motion model

Considering an adsorbate system with a periodically corrugated adsorbate-substrate potential

$$U = \sum_i u_p(r_i),\tag{1.11}$$

and the adsorbate-adsorbate interaction potential

$$V^P = \frac{1}{2}\sum_{ij} v_p(r_i - r_j),\tag{1.12}$$

where i and j represent the adsorbates pair. Besides, each one of the adsorbates felt an external force F_{ext}, starting the motion and:

$$mN_1\bar{\eta}\langle\dot{r}\rangle = NF_{ext}\tag{1.13}$$

where $\langle...\rangle$ is the thermal average, r is the coordinate of a random adsorbate, N_1 is the number of adsorbates in the first layer in direct contact with the substrate, N is the total number of adsorbates, and $\bar{\eta}$ is the sliding friction. Considering P_1 as the ratio between N_1 and N, in the case of coverage with one monolayer, $P_1 = N_1/N = 1$, but for greater coverage $P_1 < 1$. For a weak external force F_{ext}, $\bar{\eta}$ is independent of F_{ext}; this is the linear response edge. The next deduction will consider adsorbates on a (100) surface of a face-centered cubic (FCC) crystal structure. However, the generic results are not dependent on the substrate lattice structure and the specific form of U and V [17].

For a particle with coordinate $r_i(t)$, the equation of motion has the form:

$$m\ddot{r}_i + m\eta\dot{r}_i = \frac{-\partial U}{\partial r_i} - \frac{-\partial V}{\partial r_i} + f_i + F_{ext}\tag{1.14}$$

where F_{ext} is the external force, f_i is the stochastic fluctuation force expressing the influence on particle i of the irregular thermal motion of the substrate, η is the diagonal matrix with the form

$$\eta = \begin{pmatrix} \eta_{\parallel} & 0 & 0 \\ 0 & \eta_{\parallel} & 0 \\ 0 & 0 & \eta_{\perp} \end{pmatrix}.\tag{1.15}$$

The components f_i^α of f_i are linked to the friction η by the fluctuation-dissipation theorem.

$$\langle f_i^\alpha(t) f_j^\beta(0)\rangle = 2mk_BT\eta_{\alpha\beta}\delta_{ij}\delta(t).\tag{1.16}$$

Generally, the friction $\eta_\perp$ related to motion normal to the surface is much larger than the parallel friction $\eta_\parallel$. Notice that η is dependent on the adsorbate-substrate distance and the adsorbates' location on the surface. As the interaction between adsorbate-substrate is a very short range, for multilayer adsorption, to a satisfactory approximation, the friction η becomes negligible for all adsorbates, except for adsorbates in the first layer in direct contact with the substrate. The adsorbate-substrate interaction is [17]:

$$u(r) = E_B \left(e^{-2\alpha(z-z_0)} - 2e^{-\alpha(z-z_0)} \right) + U_0 \left[2 - cos(kx) - cos(ky) \right] e^{-\alpha'(z-z_0)}, \qquad (1.17)$$

where $2U_0$ is approximately the diffusion activation barrier, the wave vector $k = 2\pi/a$, with a being the lattice constant of the substrate, E_B is the adsorbate binding energy (measured experimentally), and α can be deduced from the resonance frequency for the perpendicular adsorbate-substrate vibrational mode. We will consider the substrate as rigid. With $z = z_0 + q$, where q is the coordinate of the perpendicular vibrational mode, we can deduct the quadratic order in $q : u \approx \alpha^2 E_B q^2$. The present mut be equivalent to $m\omega_\perp^2 q^2 / 2$, where $\omega_\perp$ is the vibrational resonance frequency of the vertical vibration. Thus,

$$\alpha = \left(\frac{m\omega_\perp^2}{2E_B} \right)^{\frac{1}{2}}, \qquad (1.18)$$

and knowing the resonance frequency $\omega_\parallel$ it is possible to estimate the activation barrier $2U_0$. With the Equation 1.17 is possible to derive [18]:

$$U_0 = \frac{m\omega_\parallel^2}{k^2}. \qquad (1.19)$$

The adsorbate-adsorbate interaction V is the sum of Lennard-Jones (LJ) pair potentials. The Equation 1.14 expresses the movement of an adsorbate system on a corrugated substrate. For the case where $F = 0$ the particle performs erratic movements (diffusion) with no long-term motion, for example, $\langle \dot{r}_i \rangle = 0$. With $F \neq 0$ besides the irregular motion, the particles move in the direction of F with the speed $\langle \dot{r} \rangle = F/m\overline{\eta}$. When $U_0 = 0$, the thermal average of the Equation 1.14 is:

$$m\langle \ddot{r} \rangle + m\eta_\parallel \langle \dot{r} \rangle = F, \qquad (1.20)$$

thus $\overline{\eta} = \eta_\parallel$ as supposed in this limiting approach [18].

1.3.4.2 The origin of η and f_i

In the Equation 1.14 f_i expresses the fluctuating force felt by the adsorbate i as the result of the thermal motion of the substrate ions and electrons. This force can provide the

necessary energy to the adsorbate overcomes the potential barriers, allowing the diffusion in the surface. Thermally activated movement can not occur without this term (the absence of f_i corresponds to zero temperature). In the absence of F, from Equation 1.14 until Equation 1.16, we can get $(m/2)\langle \dot{r}^2 \rangle = 3k_B T/2$, where T is the substrate temperature [18]. In the limiting case where $U = 0$ and $V = 0$ the integration of the Equation 1.14 (assuming that $\eta_{\alpha\beta} = \eta\delta_{\alpha\beta}$) is:

$$\dot{r}_i(t) = \dot{r}_i(0)e^{-\eta t} + \frac{1}{m}\int_0^t dt' e^{-\eta(t-t')}f_i(t'), \tag{1.21}$$

and with the Equation 1.16, for great times,

$$\frac{m}{2}\langle \dot{r}^2(t) \rangle = \frac{1}{2m}\int_0^t dt'dt'' 2mk_B T 3\eta\delta(t'-t'')e^{-\eta(2t-t'-t'')} = \frac{3}{2}k_B T, \tag{1.22}$$

that is the usual equipartition theorem for the mean square velocity. It is known that Equation 1.14 until Equation 1.16 can not be correct in the microscopic level. The friction force on an adsorbate is the result of collisions with the substrate ions and electrons. For a time scale that is long in comparison with the frequency and the duration of individual collisions, it can be written in the simple form $-m\eta\dot{r}$. Usually, we need to replace [18]:

$$\eta\dot{r} = \int_{-\infty}^t dt'\eta(t-t')\dot{r}(t'). \tag{1.23}$$

So, to satisfy the fluctuation-dissipation theorem, the factor f_i^α of the fluctuating force f_i must satisfy

$$\langle f_i^\alpha(t)f_j^\beta(t') \rangle = mk_B T\eta_{\alpha\beta}(t-t')\delta_{ij}. \tag{1.24}$$

The pair adsorbate-substrate nature is responsible for the time dependence of the core $\eta(t)$ (or the frequency dependence of its Fourier transform, $\eta(\omega)$). In the case which the time scale due to the pair adsorbate-substrate is shorter than the time scale linked to the motion of the adsorbate, we can change $\eta(t-t')$ by $2\eta\delta(t-t')$ or $\eta(\omega) = constant$. For this case we have again the Equation 1.14 until Equation 1.16. For adsorbates on surfaces, is the combination between the adsorbate and the vibrational (phonon) and electronic excitations of the substrate responsible for the friction η and the fluctuating force f_i [18].

The combination connected to the electronic excitations results in a frequency-independent friction and thus, local, $\eta(t-t') \approx 2\eta\delta(t-t')$ [17]. The combination connected to the substrate phonons can also result in frequency-independent friction if the frequencies associated with the adsorbate motion are minimal compared to the highest substrate phonon frequency [30]. If the characteristic frequencies caused by the motion of the adsorbate are much lower then the maximum phonon frequency ω_c of the solid, the elastic

continuum model can be applied to friction calculation, which gives the form $-m\eta v$. For physisorption systems, this is a good approximation [18].

$$\eta_\perp \approx \frac{3}{8\pi} \frac{m}{\rho} \left(\frac{\omega_\perp}{c_T}\right)^3 \omega_\perp, \tag{1.25}$$

and

$$\eta_\parallel \approx \frac{3}{8\pi} \frac{m}{\rho} \left(\frac{\omega_\parallel}{c_T}\right)^3 \omega_\parallel, \tag{1.26}$$

where ρ is the mass density, c_T is the substrate transverse sound velocity and

$$\omega_\parallel^2 = \frac{1}{m} \frac{\partial^2 U}{\partial^2 x}, \qquad \omega_\perp^2 = \frac{1}{m} \frac{\partial^2 U}{\partial^2 z}. \tag{1.27}$$

Considering a particle vibrating around a local minimum of $U(x)$, $w_\parallel$ is the resonance frequencies of parallel vibrations, $w_\perp$ is the resonance frequencies of the perpendicular vibrations, $\partial^2 U/\partial^2 x$ and $\partial^2 U/\partial^2 z$ are dependent on the position of the specimen. The coefficient of friction described in Equation 1.25 and Equation 1.26 are originated from one-phonon emission processes illustrated in Figure 7. The rotation described in Equation 1.25 and Equation 1.26 are valid for atoms and small molecules. For large molecules, incommensurate solid adsorbate layers, and for an ordered adsorbate overlayer, the results predicted from these equations may differ a lot compared to real results [17].

Figure 7 – Elementary processes involved in phononic friction excitation of a bulk or surface [17].
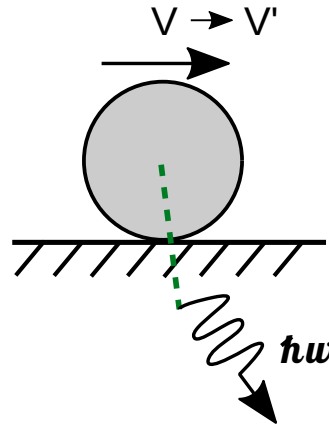
1.3.4.3   Phonon-damping of the q=0 collective adsorbate vibration

Assuming that the adsorbate unit cell is so small for all reciprocal lattice vectors G, $G > \omega_0/c_T$ where ω_0 is the adsorbate vibrational resonance frequency [18, 31–33]. For

a parallel vibration of the adsorbates to the in x-axis, with $s\hat{x}$ denoting the adsorbate displacement vector, the following relation can be written:

$$m\ddot{s} = -mw_0^2[s - u_1(0,t)], \tag{1.28}$$

where $u_1(0,t)$ is the x-component of the substrate displacement vector on adsorbate on $z = 0$. If the adsorbate lattice constant $a < \lambda$, where

$$\lambda = \frac{2\pi c_T}{\omega_0}, \tag{1.29}$$

is the wavelength of the emitted phonons. In the $q = 0$ adsorbate phonon damping calculation, the real non-uniform surface stress disposal can be a substitute for an average (uniform) distribution, leading to a uniform tangential surface stress and a consequent displacement field $u_1(z,t)$ polarized to the surface and not dependent on x and y (see the left side of the Figure 8). Solving the wave equation for the elastic displacement field $u_1(z,t)$ and applying a boundary condition, the parallel damping is

$$\eta_{\parallel} = \frac{m\omega_0^2 n_a}{\rho c_T}, \tag{1.30}$$

where n_a is the number of adsorbates per unit area. A similar procedure can be done for the $q = 0$ perpendicular adsorbate vibration, where the displacement field is polarized perpendicular to the surface and independent of x and y (see the right side of the Figure 8). Thus,

$$\eta_{\perp} = \frac{m\omega_0^2 n_a}{\rho c_L}. \tag{1.31}$$

Figure 8 – A parallel (left) and perpendicular (right) surface stress distribution generating elastic waves. The surface is uniform in space and oscillating in time. In both cases, the waves propagate orthogonally to the surface into the substrate [17].
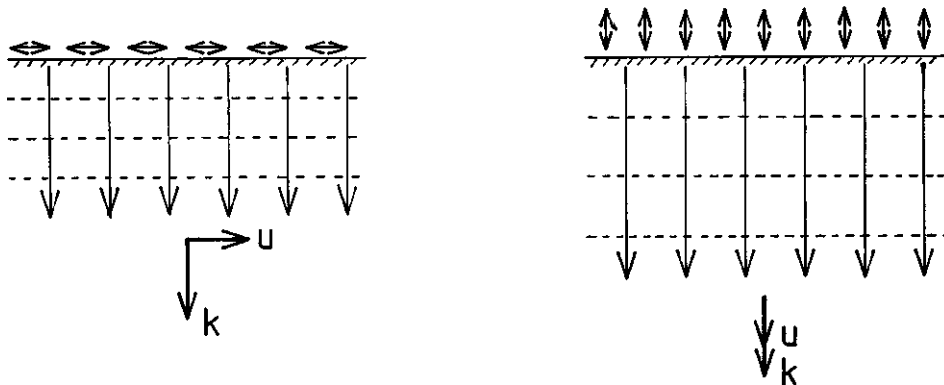
1.3.4.4   The approach proposed by Cannara et al.

Returning to the Equation 1.25, in a simplified analysis, each oscillation can be treat as a collision with the substrate. The energy transferred in the collision is $\Delta E \approx E\left(m/m_s\right)$, where m_s is the effective mass of the substrate and V is the adsorbate's vibration energy. During the collision time $\tau_c = 1/\omega_\perp$ the displacement field into the solid has a distance $\sim c_T \tau_c = c_T/\omega_\perp$. The effective mass of the substrate is the mass contained in a volume element $\Delta V \sim \left(c_T/\omega_\perp\right)^3$. Hence, $m_s \sim \rho\left(c_T/\omega_\perp\right)^3$ [17].

Considering that collision with the substrate will occur with a frequency $\nu = \omega_\perp/2\pi$, the energy transfer per unit time is

$$\frac{\partial E}{\partial t} \approx -\frac{\omega_\perp}{2\pi}\frac{m}{m_s}E, \tag{1.32}$$

resulting in a exponential decay, with damping constant $\eta_\perp$ equal to [17]:

$$\frac{\omega_\perp}{2\pi}\frac{m}{m_s} = \frac{m\omega_\perp^4}{2\pi\rho c_T^3}. \tag{1.33}$$

As a result of $\omega_\perp \propto \mu_r^{-\frac{1}{2}}$, the damping constant, the interfacial friction and the friction force all scale as $m/\mu_r^2 \approx 1/m$ [9], where m is the adsorbate mass and μ_r is the reduced mass of the system.

1.3.4.5   Objections to the model proposed by Cannara et al.

In a subsequent work made by Mo et al. [19] some objections to the model proposed by Cannara et al. [9] were presented.

The argument proposed by Cannara et al. [9] uses the vibrational damping model to explain the obtained experimental results, exalting the fact that lighter isotopes collide more frequently with the counterface, increasing friction. It has been pointed out that, despite the increased collision frequency for lighter atoms, the smaller momentum transfer in each collision should render this mass effect ineffective in reducing friction, as pointed out by Mo et al. Moreover, in the theory of the adsorbed layers, the adsorbed layer is less stiff then the substrate, which is not the case for a rigid C-H bond [19].

Another argument presented is that damping models predict that the friction disappears at small sliding velocities, which is no the real behavior of solid-solid interfaces that exhibit static friction and weak dependence of kinetic friction on velocity. Furthermore, the experimentally measured shear stress for diamond is six orders of magnitudes bigger than the estimated shear stresses by vibrational damping models. The calculation procedure was questioned because of the use of one value for the mass when estimating the kinetic energy (which controls the collision frequencies) and another value when calculating the momentum transfer [19].

Mo et al. [19] thus proposed that the effect observed by Cannara et al. can be explained by small differences, around 2 %, in surface coverage, which depends on the relative thermal stability of H- and D- passivated surfaces.

1.4 Molecular dynamics simulations

In a molecular dynamics (MD) simulation, the interactions between atoms are modeled by Newton's equations (or correspondent equations), which uses an empirical model (interatomic potential) that describes the interactions between those atoms. Each atom, or a group of atoms, is considered a unique particle with mass and charge. The Equation 1.34 shows the relation among these terms:

$$F = ma, \tag{1.34}$$

where F is the force on each atom, m is the atomic mass a is the atomic acceleration. The Equation 1.34 can be written as follow:

$$-\nabla D = m(\partial^2 r/\partial t^2), \tag{1.35}$$

where D is the potential energy felt by each atom, r is the atomic position, and t is the time. The forces acting on a particle are calculated, and the particle steps a brief increment ∂t (time step) in time as a result of these forces. This procedure is repeated for all atoms in the system during a limited number of time steps. By time-integrating the acceleration is possible to fetch the velocity, and by time-integrating the velocity is possible to fetch the position.

Both equations are solved numerically, having the necessity of discretizing the problem by dividing the domain into small steps Δt and approximating the area of the function inner each portion. The choice of Δt is a balance between the approximation error and the computational costs. The most common and straightforward numerical strategies for time-integration are the Velocity Verlet and the Leapfrog algorithms. Other examples are Adams, and the Nordsieck methods [20, 34, 35].

1.4.1 Interatomic potentials

The choice of the potential depends on the scope of the investigation. Some potentials are more generic than others, and the principle is to find candidates that describe the desired material properties, choosing the effortless [36]. A good example of generic empirical potential is the Lennard-Jones potential (LJ) [37], proposed by John Edward Lennard-Jones in 1924. The LJ potential only describes the van der Waals

interactions and the Pauli repulsion forces, according to the following relation:

$$V(r) = 4\epsilon \left[\left(\frac{\sigma_D}{r} \right)^{12} - \left(\frac{\sigma_D}{r} \right)^{6} \right],$$

(1.36)

where σ_D is a constant that represents the distance where the interatomic potential is zero, ϵ is the energy well depth, r is the inter-atomic distance. The first term describes the Pauli repulsion at a very short distance, and the second term describes the van der Waals interactions. These generic potentials are very computationally efficient, but on the other hand, fail to capture some properties of real materials [20, 36].

In general, MD of atomic friction uses three kinds of materials: metals, ionic compounds, and covalent materials [36]. Embedded Atom Method (EAM) [38, 39] takes account of the interatomic interaction between two atoms and between an atom and the free electrons. This potential is commonly used for metals [36]. Ionic materials have the necessity of considering long-range interactions (Coulomb forces), increasing computational costs. Covalent materials have directional bonds formed by valence electrons; one example of potential for this kind of material is the Stillinger-Weber [40]. The bond-order potentials were created by adding a bond-order parameter that enables evaluating the strength of different bonds simultaneously by one potential. Whereas the computational cost of bond-order potentials are high and parallel implementations are regularly used [36]. Bond-order potentials will be emphasized in the next topic because they are largely used in MD simulations with carbon.

1.4.1.1 Interatomic potentials for carbon

The first potential developed for carbon was the Tersoff potential [41], which initially was applicable only for silicon, but after was adapted for carbon [42, 43]. Tersoff potential adjusts the strengths of the bonds based on the number of neighbors. The cutoff distance is 2.1 Å, which makes the potential fast in calculations with few atoms, but beyond 2.1 Å no interaction is computed [44].

As an extension of the Tersoff potential, the Reactive Empirical Bond-Order (REBO) potential was developed by Brenner [45], including the hydrogen and improving the radicals description. The second-generation REBO-II [46] was presented twelve years after, with a better characterization of short-range bonding. Both REBO potentials use the same cutoff function that Tersoff. Based on the REBO-II potential, the Adaptive Intermolecular REBO (AIREBO) [47][1] incorporated the long-range interaction using the LJ form with a function that shut off the long-range term at short distances, and the torsional term dependent on dihedral angle [44, 47].

The Reactive Force Field (ReaxFF) potential [48] was first focused on hydrocarbons, but after, it started to be applied to other kinds of materials, including polymers, ceramics,

---

1 AIREBO was available two years before REBO-II, but used it as a base.

and metals. Rather than chemical intuition, ReaxFF started with a generic form that was parameterized using a big database. The ReaxFF family has provided good results with proteins, catalysis, and fuel cells, but the success for solid carbon phases was not the same. An improved parameter, known as Reaxff$_{C-2013}$ was liberated in 2015 [49], improving the performance related to solid carbon phases [44].

The Charge-Optimized Many-Body (COMB) [50] only contemplated carbon on the third-generation (COMB3). COMB potentials use charge-equilibration combined with bond-order, similar to ReaxFF. Depending on the version COMB uses less computational resources than ReaxFF [51]. Diamond, graphite, and other symmetric structures were used in a step-by-step way to adjust the pure carbon terms [44].

Other interatomic potentials for carbon include the Long-range Carbon Bond-Order Potential (LCBOP) [52], the second adaptation LCBOP-II [53, 54], the Environment Dependent Interaction Potential (EDIP) [55, 56].

1.4.1.2 AIREBO Potential

The family of REBO potentials is widely used in MD simulations of friction [13, 14, 19, 57]. This section will show a brief review of the mains characteristics of this potential. The AIREBO potential differs from REBO potential by including a torsional term related to σ-bond and the van der Walls interactions [45, 47]. The form of AIREBO can be described as follows:

$$E_{ij}^{AIREBO} = E_{ij}^{REBO} + E^{LJ} + E_{ij}^{tors}, \tag{1.37}$$

where E_{ij}^{REBO} is the covalent interaction between each pair of atoms and has the form

$$E^{REBO} = V_{ij}^R(r_{ij}) + b_{ij}V_{ij}^A(r_{ij}), \tag{1.38}$$

where V_{ij}^R is the repulsive pairwise potential, and V_{ij}^A is the attractive pairwise potential of atoms i and j. Both are determined by the atom types (carbon or hydrogen) and depend on r_{ij} distance. The many-body term b_{ij} controls each term's contribution, being responsible for changes in the equilibrium conditions of the system, for example, in the limit of attraction between atoms and the bond equilibrium distance. It is related to the position and chemical identity of atoms [45, 47, 58]. The E^{LJ} term corresponds to the van der Walls interactions defined by the Lennard-Jones model, according to Equation 1.36. The system's chemical nature must be considered in resolving when to include or exclude the LJ interaction, preserving the reactive aspect of the AIREBO potential. Mathematically,

this is done by using a set of switching functions [47]:

$$E_{ij}^{LJ} = S(t_r(r_{ij}))S(t_b(b_{ij}^*))C_{ij}^S V_{ij}^{LJ}(r_{ij}) + [1 - S(t_r(r_{ij}))]C_{ij}^S V_{ij}^{LJ}(r_{ij}). \tag{1.39}$$

The C_{ij}^S term based on the interaction between atoms i and j is used for evaluating the interactions between atoms associated with the LJ potential and near neighbors, excluding the first and the second neighbors modeled by REBO potential and the third neighbor described by the torsion term. The bonding switch $S(t_r(r_{ij}))$ changes the interaction force between atoms based on LJ potential; $S(t_b(b_{ij}^*))$ filters the repulsive LJ interactions between atoms situated in longer distances than the covalent distance, but continue exerting certain contribution due to the number of neighbors [47, 58]. E_{ij}^{tors} is the torsional term dependent on dihedral angles and has the form [47]:

$$E_{ij}^{tors} = \frac{1}{2} \sum_i \sum_{j \neq i} \sum_{k \neq i,j} \sum_{l \neq i,j,k} w_{ij}(r_{ij})w_{jk}(r_{jk})w_{kl}(r_{kl}) \times V^{tors}(w_{ijkl}), \tag{1.40}$$

where:

$$V^{tors}(w) = \epsilon \left[\frac{256}{405} cos^{10} \left(\frac{w}{2} \right) - \frac{1}{10} \right]. \tag{1.41}$$

The use of bond weights such as $w_{ij}(r_{ij})$ ensures that the torsional energy associated with a given dihedral angle w_{ij} can be removed without problems when any of the constituents of the bonds is broken [47].

1.4.2 Periodic Boundary Conditions

Typically, the simulated systems sizes are tiny compared to a real system, and some effects due to the finite size can affect the results. One way to minimize these effects is using periodic boundary conditions (PBC), with the aim of simulating an infinite system size using a finite system size [59]. There are many ways to treat atoms in the system boundaries: no boundary conditions mean that the atoms will pass through the boundary; reflecting boundary conditions mean that the atoms will be redirected by changing the velocity sign; periodic boundary conditions mean that the atoms crossing the boundary will reappear in the other side of the simulation box. More specific points may be included due to boundary conditions [20]. Figure 9 demonstrates the concept of PBC for a two-dimensional (2D) system.

When using PBCs, we may consider the wraparound effect, which is applying minimum image convention when computing quantities that are dependent on position [20, 60]. An example of a minimum image convention for a 2D system is shown in Figure 10, where one replica of the blue atom is closer to the red atom than the original blue atom.

Figure 9 – Periodic boundary condition concept for a 2D case [60].
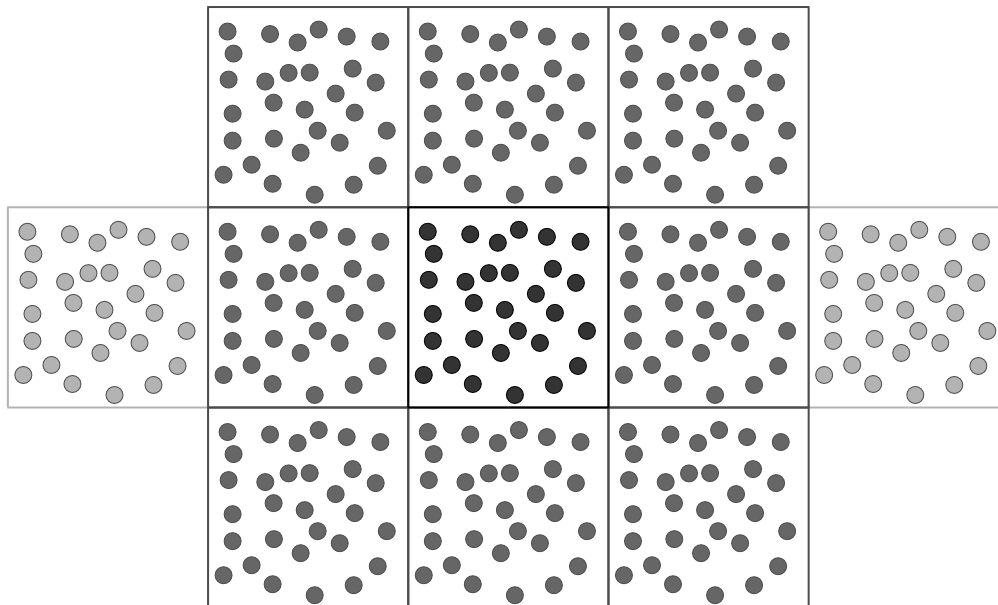
Figure 10 – Minimum image convention for a 2D system. The shortest distance between the red atom and the blue one is indicated with an arrow [20].
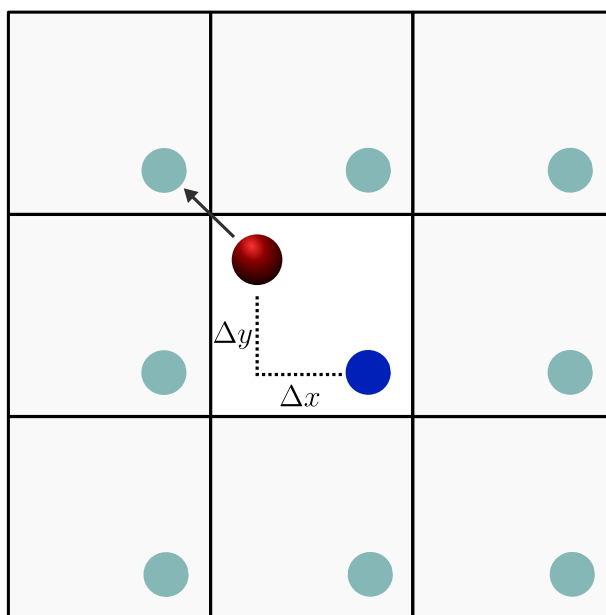
1.4.3   Ensembles

MD simulations form a microcanonical NVE ensemble in statistical mechanical terms when the number of particles N, the volume V, and the energy E are constant (equations of motion correspond to a conservative system). A constant-temperature experiment coincides with a canonical (NVT) ensemble, which has the number of particles N, the volume V, and the temperature T constant. The constant pressure can be introduced,

generating the isothermal-isobaric (NPT) ensemble, which has the number of particles N, the pressure P, and the temperature T constant. We can model the ensemble conditions according to the system in study [60,61].

1.4.4 Extracting physical quantities

1.4.4.1 Energy

The kinetic energy is calculated classically,

$$E_K = \frac{1}{2}\sum_{i=1}^{N} m_i v_i^2, \tag{1.42}$$

where v_i is the velocity and m_i is the mass of the particle. The potential energy, dependent on the used potential, is calculated as

$$E_P = \sum_{i=1}^{N}\sum_{j>i}^{N} U(r_i, r_j), \tag{1.43}$$

where U is dependent on potential, r_i is the relative position of the atom i, and r_j is the relative position of atom j [20,60].

1.4.4.2 Pressure

Usually, the pressure calculation is performed by the virial route [62]. For a NVT system with volume V and particle density $\rho = \frac{N}{V}$, the pressure can be calculated by the following equation:

$$P = \rho k_B T + \frac{1}{dV}\left\langle \sum_{i<j} F_{ij} \cdot r_{ij} \right\rangle, \tag{1.44}$$

where d is the number of dimensions, F_{ij} is the force experienced on atom i from atom j located at r_{ij} relative distance to atom i. This is a method that assumes a NVT ensemble. For a NVE ensemble, the relation is not the same [20]. In a system with pairwise interactions, the first term on the right-hand side of Equation 1.44 is the ideal gas kinetic contribution, and the second term is related to the residual contributions originating from the interactions [62].

1.4.4.3 Temperature

According to statistical thermodynamics, the thermal energy of a system is given by:

$$E_K = \frac{f_D}{2} N k_B T, \tag{1.45}$$

where N is the number of particles, k_B is the constant of Boltzmann, f_D is the kinetic degrees of freedom and T is the temperature [61]. As we treat each particle as a point, rotational degrees of freedom are neglected (only translational degrees of freedom are used). Assuming Newtonian motion, we can use Equation 1.42 and find the relation for the instantaneous temperature

$$T = \frac{\langle m_i v_{i^2} \rangle}{f_D k_B},\tag{1.46}$$

which approximates the instantaneous temperature by the particle's velocities, oscillating around the real temperature value (time-averaging is adopted when computing the value). The use of thermostats can control the system temperature [20].

1.4.5 Nosé-Hoover Thermostat

A variety of thermostats are available for controlling the temperature of the simulated system. An amount of them controls the temperature adjusting the particles' velocity (see Equation 1.46), for example, in the Berendsen [63] and the Andersen [64] thermostats. These kinds of thermostats are good options for equilibrating systems However, due to the direct velocity rescale, they can lead to inconsistencies in the simulations [20,61]. The Nosé-Hoover [65–67] thermostat adds an imaginary friction force, changing the Hamiltonian of the system. The original equation of motion,

$$F_i = -\nabla U_i(r^N),\tag{1.47}$$

becomes

$$F_i = -\nabla U_i(r^N) - \xi m v_i\tag{1.48}$$

where F_i is the force felt by a particle, U is the potential, $r^N = (r_1, r_2, ..., r^N)$ is the positions of all particles in the system, ξ is a dynamic variable that regulates the strength of the thermostat, m is the mass, and v_i is the velocity of the particle i. By working in this way, the thermostat does not rescale the velocity of particles, generating proper dynamics and realistic constant temperature conditions [20,61].

The next chapter will describe the methodology used in this work.

2 Methods

The simulated system comprises two bodies, a big slab positioned in the inferior part of the simulation box and a smaller tip (probe) in the simulation box's upper region. The molecular dynamics simulations (MD) were carried out using the Large-scale Atomic/Molecular Massively Parallel Simulator (LAMMPS) [68] with the AIREBO potential (see subsubsection 1.4.1.2 for the choice of the potential), including long-range van der Waals interaction [47]. LAMMPS is an open-source code for classical molecular dynamics simulation, focused on materials design, distributed under the terms of the GNU Public License. It was developed at Sandia National Laboratories (<https://lammps.sandia.gov/>), a US Department of Energy facility. The design was created to run efficiently on parallel computers.

In the following sections, the construction of the system will be detailed, as well as the main LAMMPS commands and syntax used to create the desired conditions.

2.1 Slab construction

The slab with dimensions 141.36 Å x 144.58 Å x 20.95 Å was created directly with a LAMMPS script by the repetition of the diamond unit cell, with [111] lattice direction oriented with the z-axis. This is the same crystallographic surface used by Cannara et al. [9] in their AFM measurements and Mo et al. [19] in their MD simulations. The *units metal* was used (for a complete view of *units metal*, please see Appendix A). Periodic boundary conditions were imposed on the x and y directions but not on the z-direction (direction of the applied load). In the first part of the script, the variables connected to the system's size were defined. The command *lattice diamond*, in sync with the *orient* option, effectively built the structure (for a complete view of this script, please see Appendix B). Note that the box simulation limits were carefully defined, respecting the diamond structure and the lattice constant of 3.57 Å.

```
1  lattice diamond ${latparam} orient x 1 -1 0 orient y 1 1 -2
       orient z 1 1 1
```

Listing 2.1 – Lattice command used for the slab construction, where *latparam* is the variable of the lattice constant for diamond (3.57 Å).

With the commands *region* and *group*, the system was divided into three different regions. The upper layer received the mass of the hydrogen (1.01 g/mol), the intermediate part of the system, and the bottom one received the mass of the carbon (12.0107 g/mol).

This was useful in the work sequence when establishing specific conditions for each part of the system (see section 2.3).

```
1  mass 1 12.0107
2  mass 2 1.01
3  mass 3 12.0107
4
5  #define hydrogens
6  region top_slabHR block INF INF INF INF 1.4 1.6 units box
7  group top_slabHG region top_slabHR
8  set group top_slabHG type 2
9
10 #define  rigid  carbons  on the  base
11 region fixoR block INF INF INF INF INF -18.0 units box
12 group fixoG region fixoR
13 set group fixoG type 3
```

Listing 2.2 – Generation of the different regions.

Finally, the potential AIREBO was applied in the slab using the commands *pair_style/pair_coeff*, considering the second type of atoms as hydrogen. For creating a *dump* file, the dynamic was run just for one time step. The output *dump* was visualized on Ovito [69].

```
1  pair_style      airebo 3 1 0
2  pair_coeff      * * /opt/lammps/potentials/CH.airebo C H C
3
4  timestep 0.0002
5  dump   1 all custom 100 dump.teste.* id type xs ys zs fx fy fz vx vy vz
6
7  run 1
8  quit
```

Listing 2.3 – Applying the AIREBO potential.

For the posterior use in this work's main script, the file was exported to the LAMMPS data file format (*dat*).

2.2 Tip construction

The diamond tip (probe) with dimensions 27.27 Å x 28.47 Å x 19.36 Å was first created with a LAMMPS script by repeating the diamond unit cell, with [111] lattice direction oriented with the z-axis. In the first part of the script, the variables connected to the system's size were defined. The command *lattice diamond*, in sync with the *orient* option, effectively built the structure (for a complete view of this script, please see Appendix C).

```
1  lattice    diamond ${latparam} orient x 1 -1 0 orient y 1 1 -2
      orient z 1 1 1
```

Listing 2.4 – Lattice command used for the probe construction, where *latparam* is the variable of the lattice constant for diamond (3.57 Å).

Two different kinds of atoms were assigned in the script, carbon for the first one and hydrogen for the second one. Until this point, the procedure was very similar to the slab one. Due to the necessity of hydrogenation in a more complex structure than the slab, the *dump* file opened in Ovito was exported to the *xyz* format file (the particle's name, in this case only carbon, needs to be changed to C before saving the file). The *xyz* file was opened in Gabedit (<http://gabedit.sourceforge.net/>) software, which has the functionality of hydrogenation.

For the posterior use in this work's main script, the file was exported to the LAMMPS data file format (*dat*).

2.3   The simulated system

This section will present the main points about the input script used during the study. The entire script with comments is available in Appendix D. It is recommended a brief visualization of this appendix for a better understanding of the LAMMPS commands and the logic used in the construction of the script.

The slab of thickness 20.95 Å was divided in three distinct regions [36], as shown in Figure 11. The bottom region, consisting of 1 atomic layer, was treated as a rigid plate after the relaxation of atomic positions and was used to drag the whole sample during the friction simulations. The second region consisted of 5 atomic layers, which were simulated in a NVT ensemble. The top region consisted of 4 atomic layers in a NVE ensemble. The size of the periodic cell representing the diamond surface and the number of atomic planes in each of above mentioned three layers was chosen to keep the computational cost of the MD simulations within reasonable limits, thus allowing to follow the dynamics of the system for as long as 120 ps. Just like a mirrored sample slab, the probe block consisted of three distinct regions.

2.3.1   Temperature

In general, in MD simulations of atomic friction, the thermostat is not applied in the contact area, avoiding changes in the studied area dynamics [34]. The thermostat is applied in layers far from the surfaces, both for the tip and substrate, providing a good heat dissipation [36]. In this work, we used a Nose-Hoover thermostat with friction factor

Figure 11 – Schematic representation of the simulated system, including the probe (on top) and part of the diamond substrate. Carbon and hydrogen atoms are represented as dark gray and light gray spheres, respectively. The probe is attached to a fixed point by a spring (top right).
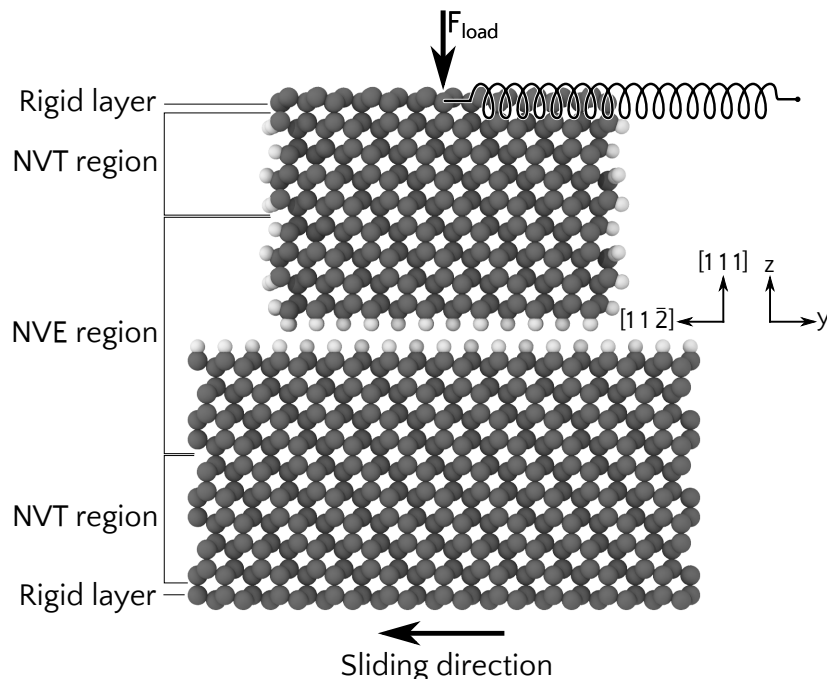
0.5 ps to hold the NVT regions in the tip and substrate at 10 Kelvin, providing a thermal bath to the system (please refer to Figure 11 to regions disposal).

Except for a few tests performed at 300 K to evaluate the influence of temperature on the simulations with different surface coverage, the coupling to the NVT regions allowed us to carry out the MD simulations at 10 K. At such low temperatures, the relaxation of the simulated diamond surfaces is very much hindered, and in the absence of surface reconstruction, the influence on the friction of the different surface modifications here explored should be significantly enhanced The *compute temp/com* command was used to calculate the temperature of all the dynamics atoms on the system (fixed atoms not included) after discounting out the center-of-mass velocity of the group.

```
1 compute temp_dinamico dinamicoG temp/com
2 thermo_modify temp temp_dinamico
3
4 fix fixnvtblocoID nvtblocoG nvt temp ${T} ${T} 0.5
5 fix fixnvtslabID nvtslabG nvt temp ${T} ${T} 0.5
6
7 fix fixnveblocoID nveblocoG nve
8 fix fixnveslabID nveslabG nve
```

Listing 2.5 – Main commands used for temperature control. The variable ${T} stores the desired temperature.

2.3.2   Applying load

In MD simulations of friction, the normal force can be applied to the tip's superior atoms, usually treated as a rigid body, or by imposing a constant distance between the tip and the substrate [36]. To the top rigid layer of atoms of the probe, we applied a uniform force in the z-direction, see Figure 11 (considered a better alternative than imposing a constant distance between the tip and substrate [15]).

The *fix addforce* applies a fz component of force for each atom in the group. To hold the superior atoms as a rigid body, we used the LAMMPS command *fix rigid.*

```
1 fix rigidBlockID top_blockG rigid single force 1 off on on torque 1 off
    off off
2 fix fix_forca_normalID top_blockG addforce 0.0 0.0 ${F_normal}
```

Listing 2.6 – Fix commands for making a rigid body and to apply a fz component of force. The *F_normal* is the variable that defines the value of fz force per atom.

2.3.3   Measuring lateral force

A massless spring with force constant $k_m = 3\,\mathrm{eV}\,\text{Å}^{-2}$ was attached in the rigid atoms of the probe between the center of mass of the tip and a tether point. Only the y components of deformations of the spring result in a force (the spring is free to move without resistance on the xz-plane). To define the k_m value, we can set $k_m y$ with the same value of the cantilever or, in a more accurate treatment, specify the stiffness as the same value of the effective experimental stiffness. Alternatively, we can directly vary the spring stiffness until the aimed effective stiffness is achieved [36]. The average value of the measured lateral force decreases as the spring stiffness increases, while the maximum values of lateral forces obtained increase [70]. Tests conducted with stiffer springs attached to the probe revealed an increase in the frequency of the instantaneous friction force oscillations while the amplitude is less influenced by the spring constant. For larger spring constants, the periodicity of the instantaneous friction force matches the distance between maxima in the potential energy.

2.3.4   The probe orientation

The relative positions of the atoms in the contact interface have an important effect on atomic friction. Two different orientations of the probe relative to the sample were considered. In condition #1, the crystallographic directions of the probe and the sample are perfectly aligned, and the -y and z directions of the lab reference of the frame are respectively aligned with the [11$\bar{2}$] and [111] crystallographic directions. In condition #2, the sample is kept in place while the probe is rotated about the z-axis, and its [11$\bar{2}$] crystallographic direction forms an angle of 15° with the -y axis. The condition #2

originates what is called structural lubricity[1], which comes from the fact that, at any given time, the interaction forces between tip and substrate in different directions counteract each other, and there is a small net force or, equivalently, a shallow potential energy landscape [36, 71]. In the final script, this is done by the use of the LAMMPS command *displace_atoms* with style *rotate*.

```
1 displace_atoms blockG rotate 12.6111 13.106 0.0 0 0 1 ${rotation_angle}
```

Listing 2.7 – The rotational command used to rotate the tip, where *rotation_angle* is the variable defined at the beginning of the script.

2.3.5   Influence of the mass

The effect of the atomic mass of the adsorbate was explored by artificially changing the H atomic mass from 1 u to 16 u, while keeping its chemical nature (i.e., the interatomic potential) unaltered. The upper limit of 16 u is obviously way beyond the experimental possibilities and was chosen to exacerbate any mass-effect on friction.

2.3.6   Influence of the coverage

The effect of adsorbate coverage on friction was assessed by performing simulations for three different conditions. Firstly, (i) the degrees of surface coverage were varied down to 80 %, in which case 20 % of the adsorbate atoms were randomly removed from the sample. The probe surface was kept 100 % passivated. In (ii), an extreme case was proposed. In order to hinder the effect of lateral momentum transfer, we removed 88 % of the H atoms from the surface in an orderly fashion (12 % coverage), both on the sample and the probe, see Figure 12. In this case, the transfer of momentum is limited to occur almost exclusively along the C-H bonds (perpendicular to the plane of sliding) and lateral momentum transfer between hydrogen atoms at the same surface is virtually eliminated. Additionally, in (iii), to evaluate the effect of carbon dangling bonds on friction, simulations were performed in which carbon atoms substituted 20 % of the hydrogens both on the sample surface and on the counterface.

2.3.7   The dynamics

In each of the studied cases, the system was relaxed before the start of the MD simulation by minimizing the energy until convergence to within 1 part in 10 000 and by assuring that none of the cartesian components of the force on any of the atoms was greater than $0.1 \, \mathrm{meV \, \mathring{A}^{-1}}$. After relaxation of the whole system with the probe block maintained at a distance of 9 Å from the slab surface, the probe was allowed to approach the sample surface and the system was let to equilibrate during 60 000 steps (each time

---

[1]   It has also been called "superlubricity".

Figure 12 – Slab surface with 80 % of the H atoms removed, limiting the transfer of momentum along the C-H bonds.
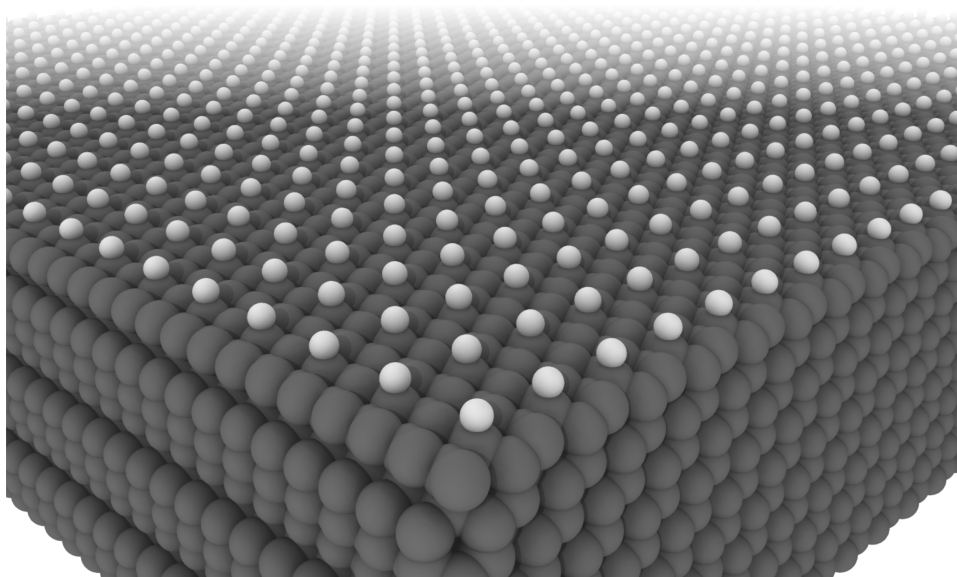
step corresponds to 0.1 fs) with the chosen applied load F_{load}. After that, the sample begins to move in the -y direction ([11$\bar{2}$] crystallographic direction) at $1.0\,\text{Å}\,\text{ps}^{-1}$. The system is let to evolve for a period between 2.6 ps and 42 ps, depending on the time needed to reach steady-state. Once the system is in a steady-state regime, the production phase begins and lasts for a minimum of 36 ps in order to sample at least four friction force cycles. Each simulation had a total of 1 200 000 time steps. At each 200 time steps the y-component of the force on the spring, the position of the center of mass of the probe block, and the temperature of the NVE ensemble are recorded.

2.3.8   Evaluating the density of vibrational states

We chose a pair of atoms C-H far from the tip. Therefore, the applied normal force may have small effects or no effects in the results. With the assumption that these two atoms' velocities are the result of the entire system, then we can consider this pair of atoms to evaluate the vibrational modes of the C-H bonding. For the analysis, we rerun 5000 steps after the system's initial equilibration, generating a *dump* file of this pair of atoms at each time step. The vibrational density of states was calculated using Trajectory Analyzer and Visualizer - TRAVIS (<http://www.travis-analyzer.de/>) using the resources available and described in the the software's documentation [72–74].

2.3.9   Data analysis

Data analysis was implemented in Python language, using Jupyter notebooks [75,76], see section 3.8. Curve fittings were performed using LMFIT [77]. Uncertainties in the fitting parameters and combined uncertainties in physical quantities were estimated using the UNCERTAINTIES package [78]. The instantaneous friction force exhibits periodic oscillations, more or less defined depending on the conditions being simulated, as shown in the next section. Accordingly, the instantaneous lateral force was time-averaged over each cycle of force oscillation and the overall friction force was obtained as the average of the set of averages calculated for each complete cycle. The uncertainty of friction force was estimated as the standard deviation of the set of average friction forces over each cycle. The slope of the straight line fitted to the friction force *versus* normal force data yields the corresponding coefficient of friction.

2.3.10   Computational resources

All the calculations were performed in two supercomputers: the Gauss computer from the Centro Nacional de Supercomputação (CESUP) and the SGI ICE-X (Lobo Carneiro) computer from the Núcleo Avançado de Computação de Alto Desempenho (NACAD). The supercomputer Gauss has one connection unit and 64 processing units. Each one has 64 GB of Random Access Memory (RAM) and 2 dodeca core AMD Opteron processors (32 units with 6176 SE model and 32 units with 6238 model, operating in 2.3 GHz and 2.9 GHz, respectively). There are 1536 processing cores with a theoretical performance of 24 TFlops (simple precision). The supercomputer Lobo Carneiro has 504 CPUs Intel Xeon E5-2670v3 (Haswell), totaling 6048 Cores. The cores are divided into 252 nodes with 24 cores each (with the possibility of using Hyper-Threading (HT)). Each node has 64 GB of RAM.

The next chapter will describe the main results obtained in this work.

Part II

Results and Discussion

3 Results and Discussion

The three first subsections of this chapter present the general results obtained in the simulations, followed by the topics connected to the specific conditions proposed in the methodology. By the end, access to the data is shown.

3.1 Density of vibrational states

Figure 13 presents the behavior of the vibrational states as a function of the adsorbate mass for the masses 1, 2, and 4 u.

Figure 13 – Vibrational density of states as a function of the adsorbate mass.
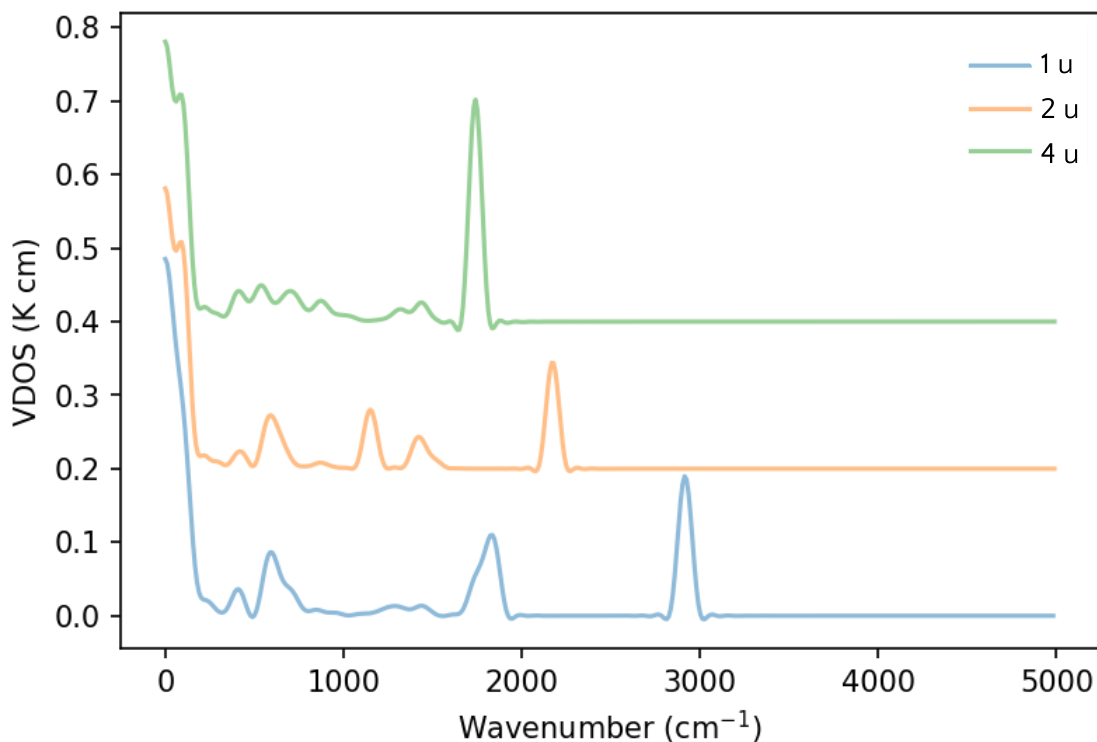
The peak around 2900 cm^{-1} corresponds to the C-H bond experimental results [79, 80]. By increasing the adsorbate mass, the peak is offset to a smaller wavenumber, as expected. With these results, we can consider that our system can simulate and capture differences in the vibrational states, which is the main element of the phononic friction.

3.2   Influence of the probe orientation

The potential energy as a function of lateral displacement on the -y direction is shown in Figure 14 for conditions #1 and #2. The curves were obtained by fixing the distance between the hydrogen atoms from the tip and the sample at 1.6 Å. In condition #1, the atomic arrangements of the tip and the sample are commensurate, yielding a periodic potential energy curve with large amplitude, the distance between maxima corresponding to the distance between H rows in the [11$\bar{2}$] direction. In this case, the higher potential energy maxima correspond to the H atoms of the tip passing over the H atoms of substrate (interplanar distance B represented in Figure 14), while lower maxima correspond to the tip atoms passing in-between the substrate atoms (interplanar distance A represented in Figure 14; see also movie M1 in Supplementary Material). In condition #2, in which the tip is rotated by 15°, the atoms revolve around each other in all directions on the plane of the interface yielding a condition known as structural lubricity [81, 82].

Figure 14 – Potential energy *versus* lateral displacement for the conditions #1 and #2 explored in this work. Curves are labelled according to the angle between the [11$\bar{2}$] crystallographic directions of the tip and the direction of sliding over the passivated diamond surface. Superimposed images illustrate a top view of the system (sample + probe), with the chemisorbed atoms on the sample's substrate and on the tip's surface represented in light and dark color, respectively. Conditions #1 and #2 discussed in the text are represented at left and at right, respectively. The red arrow indicates the direction of sliding (-y direction in the laboratory frame of reference and [1 1 $\bar{2}$] crystallographic direction of the sample). A and B indicate the interplanar distances discussed in the text.
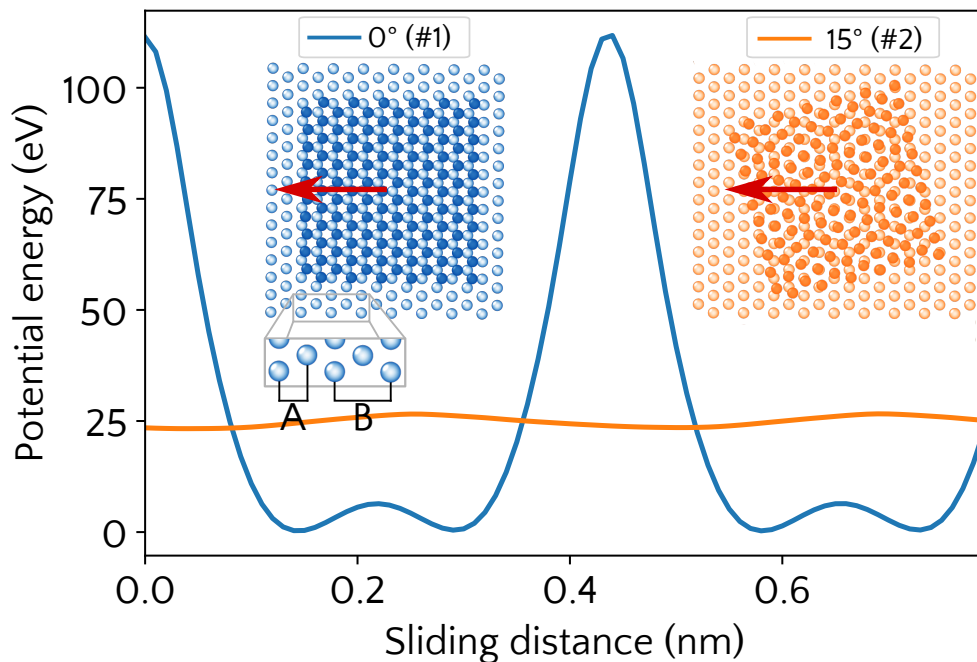
For simulations in condition #1, the friction force exhibited well-defined, periodic

oscillations, as shown in Figure 15. For normal forces of 33 nN and above, the sliding surfaces exhibit a characteristic stick-slip effect (see animation M2 in the Supplementary Material).

Figure 15 – The instantaneous force on the spring attached to the tip as a function of the sliding distance for condition #1 and #2 and 198 nN normal force.
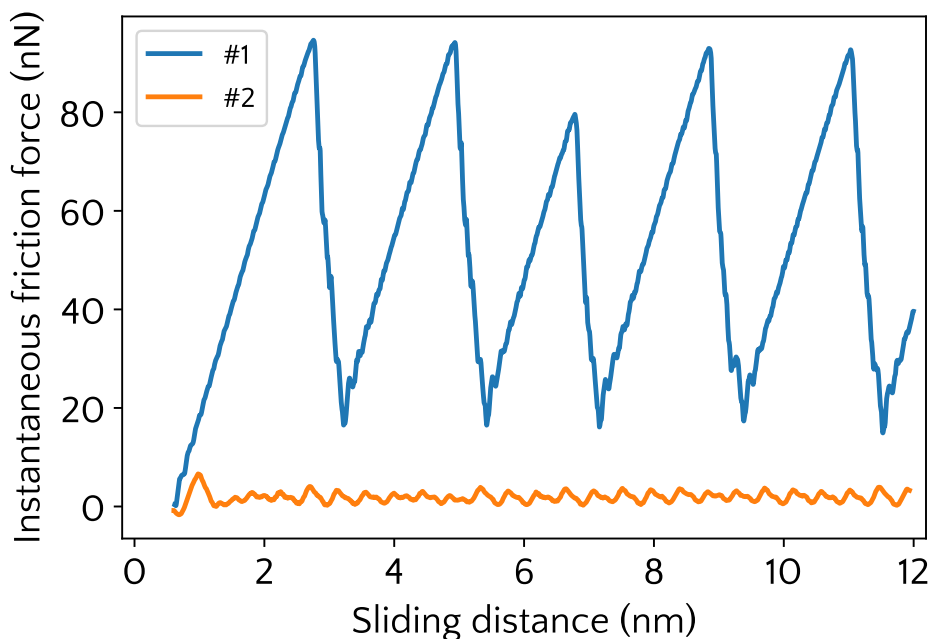
It is also possible to visualize in Figure 15 the difference between the measured instantaneous friction force level. When sliding in condition #2, the periodic stick-slip behavior disappears for all normal loads evaluated, an example of which is shown in Figure 16. Indeed, rotation of the probe relative to the sample (and relative to the direction of movement, for that matter), gives rise to a condition of structural lubricity. In this case, the contribution of individual surface atoms are averaged out to a small amplitude of oscillation of the net friction force, as already commented above.

3.3 General findings

Even though the sliding velocity in our MD simulations is five times greater than the $20 \, \mathrm{m \, s^{-1}}$ of the study performed by Mo et al. [19], and orders of magnitude higher than the sliding velocity of an AFM tip in typical experiments (approximately $1.2 \, \mathrm{\mu m \, s^{-1}}$), it is still less than 1 % of the speed of sound in diamond, and compatible with speeds used in similar simulations [83]. Additionally, temperature gradients promoted by the relative sliding of the tip and the surface were small in all simulations. The contact pressures between the tip probe and the diamond surface varied in the interval from near zero up to around 75 GPa. In spite of the relatively high maximum contact pressures (in

Figure 16 – The instantaneous force on the spring attached to the tip as a function of the sliding distance for condition #2 and 495 nN normal force. The periodic stick-slip behavior disappears for all normal loads applied in sliding condition #2.
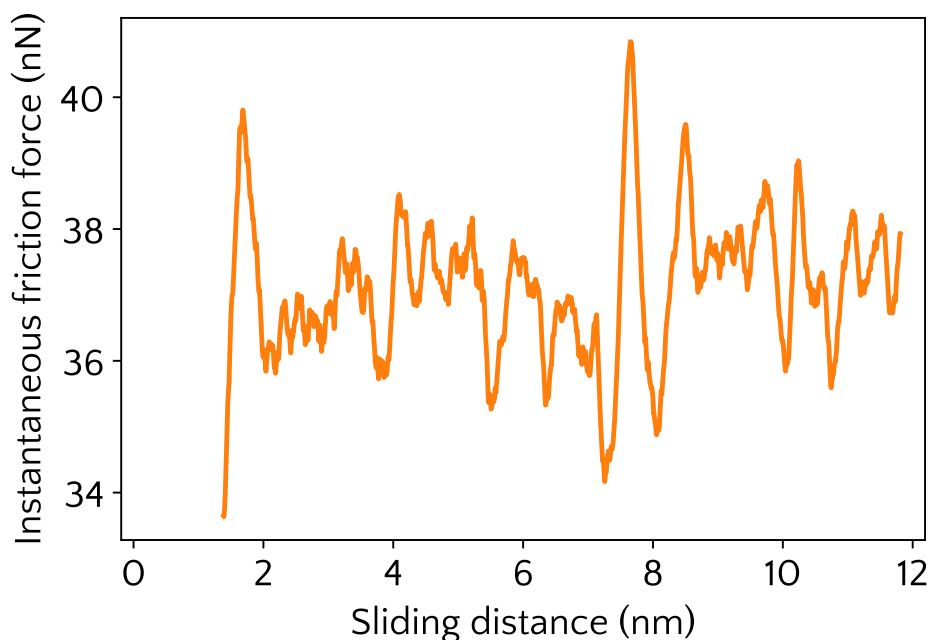
comparison, for instance, with $6.12\,\mathrm{GPa}$ in the work by Mo et al., and around $5.0\,\mathrm{GPa}$ in AFM experiments [19]), it is not unusual for MD simulations of friction. Gao et al., for instance, have reached contact pressures around $64\,\mathrm{GPa}$ in their simulations of friction in diamond using a flat counterface [14]. In our simulations, no plastic deformation of the diamond surface nor atom detachment from the sliding surfaces were observed (see movie M3 in the Supplementary Material showing the system under conditions of maximum contact pressure).

3.4   The effect of varying the atomic mass of the surface atoms

For both conditions #1 and #2, a linear dependence of friction force on applied load was observed (see Figure 17 and Figure 18, respectively), in agreement with previous simulations using the REBO potential [14]. In fact, there was no apparent influence of normal force on the coefficient of friction (nor any hint of a change of friction mechanism) in the range of contact pressures here explored. In the regime of larger normal forces evaluated for condition #2, the atoms of the counterface accommodate in the interstices of the adsorbate atoms on the sample. When sliding begins, the adsorbate atoms revolve over each other, activating the bending modes of the C-H bonds and transferring momentum to the neighboring atoms, which causes the coefficient of friction to increase (see movies

Figure 17 – Friction force as a function of normal load for sliding in the condition #1, for different masses of the chemisorbed atoms (in atomic mass units). The continuous lines represent linear fits to the data.
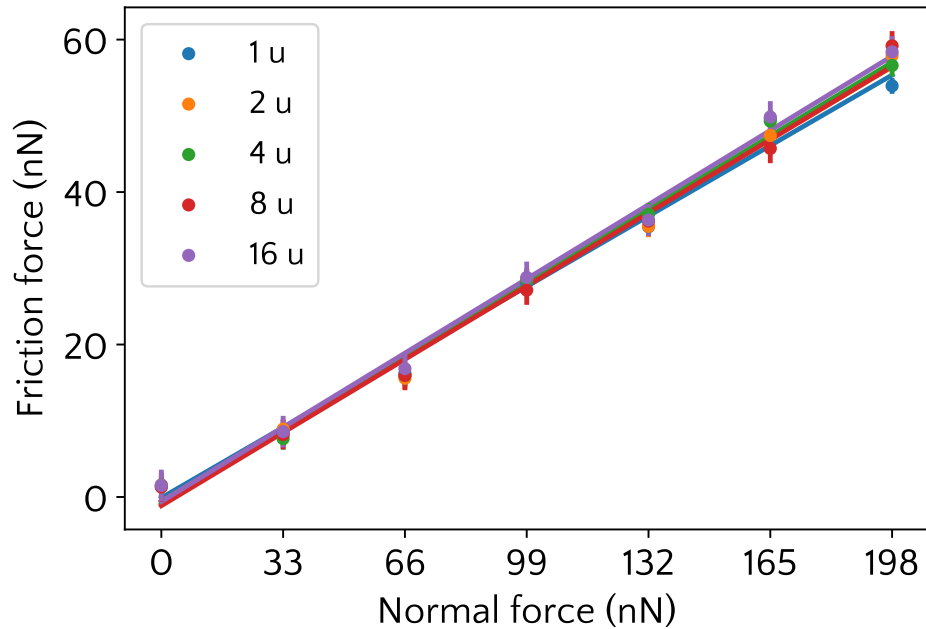
Figure 18 – Friction force as a function of normal load for sliding in the condition #2, for different masses of the chemisorbed atoms (in atomic mass units). The continuous lines represent linear fits to the data. Error bars are not visible on the graph due to their small size concerning the y-axis scale.
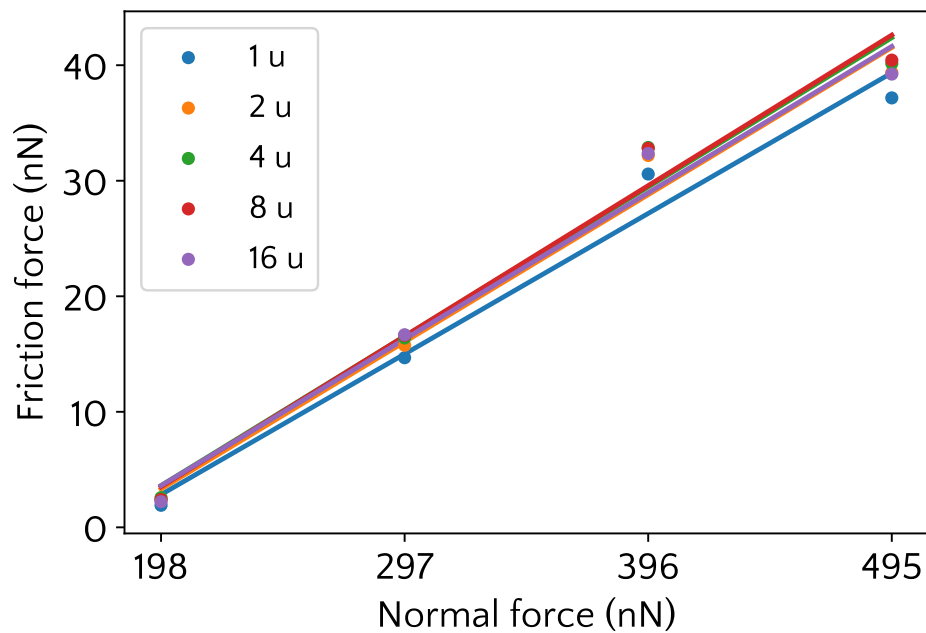
M4 and M5 in Supplementary Material). This same effect has been observed in computer simulations as early as 1993 by Harrison et al. [84] and, more recently, by Gao et al. [14,28]. For lower loads, a smaller coefficient of friction is expected. In this regime of contact pressures, extensively described by Dong et al. on graphene surfaces [82], the atoms of the surface and counterface interact only superficially and easily glide over each other (see movies M6 and M7 in Supplementary Material).

Figure 19 – The coefficient of friction as a function of adsorbate mass for sliding in condition #1. The continuous lines represent linear fits to the data. Dark and light gray bands are the 1σ and 2σ prediction intervals, respectively. The green line in the inset graph represents the expected behavior for the coefficient of friction according to the approach proposed by Cannara *et al.* [9]. Error bars are not visible on the inset graph due to their small size concerning the y-axis scale.
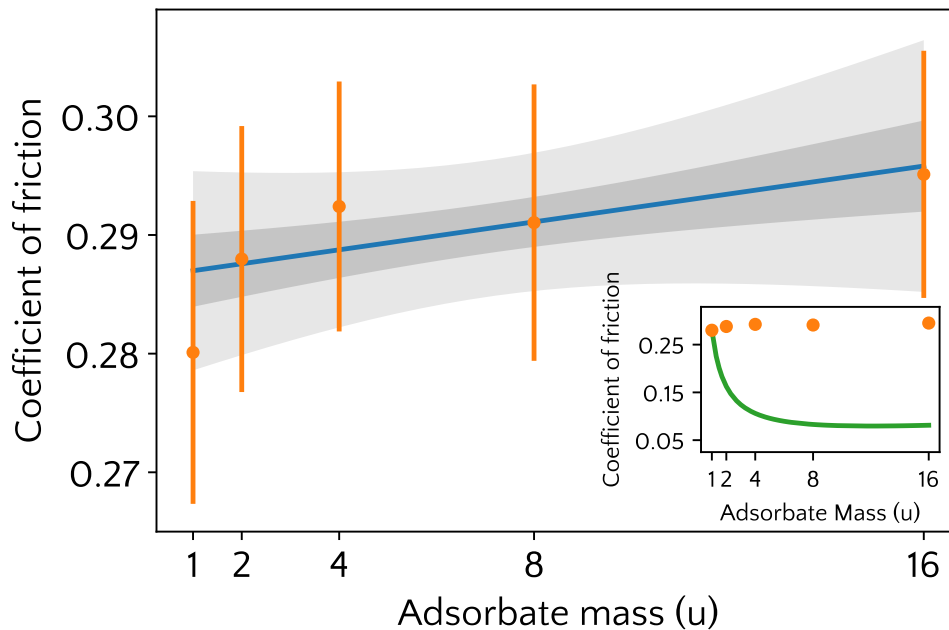
The coefficients of friction as a function of adsorbate atomic mass for conditions #1 and #2 are shown in Figure 19 and Figure 20, respectively. The slight increase tendency of the coefficient of friction by increasing the adsorbate atomic mass is contrary to that expected according to the energy-transfer model of Cannara et al. [9] (see inset graphs on Figure 19 and Figure 20), which predicts a reduction in the coefficient of friction following a m/μ_r^2 dependency. In fact, the results depicted in Figure 19 and Figure 20 are compatible, at a 0.05 significance level, with the hypothesis that the coefficient of friction is independent of the adsorbate atomic mass for both sliding conditions #1 and #2. This observation in on par with the results from MD simulations by Mo et al. [19], who attributed the decrease in friction by substituting deuterium for hydrogen in AFM experiments performed in ultra-high vacuum [9] to differences in surface coverage caused

Figure 20 – The coefficient of friction as a function of adsorbate mass for sliding in condition #2. The continuous lines represent linear fits to the data. Dark and light gray bands are the 1σ and 2σ prediction intervals, respectively. The green line in the inset graph represents the expected behavior for the coefficient of friction according to the approach proposed by Cannara *et al.* [9].
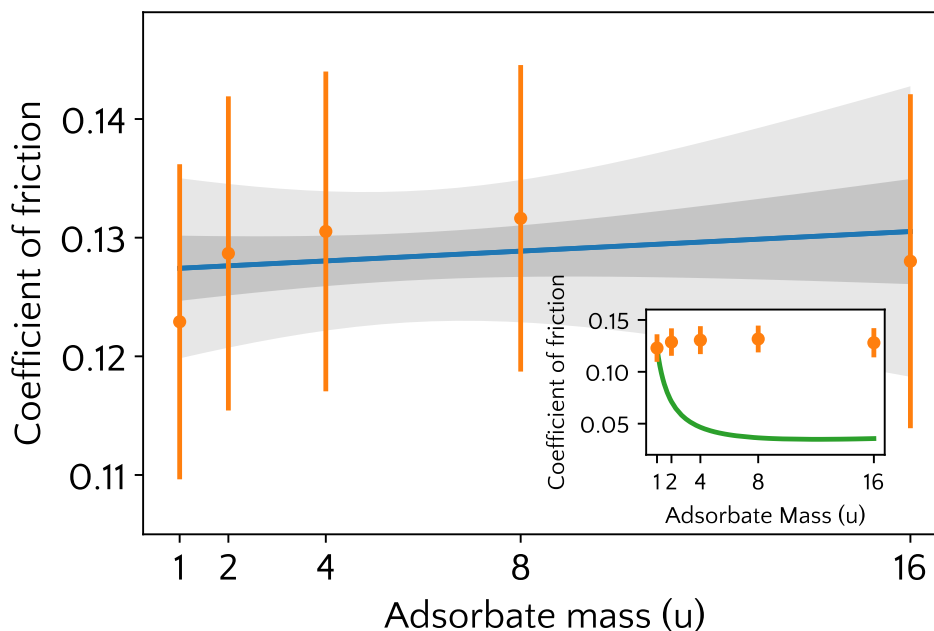
by different desorption rates of H and D from the diamond surface. Furthermore, it must be pointed out that no hydrogen exchange between sample and probe surfaces was observed in the conditions here simulated for all totally or partially H-passivated surfaces (see, for example, animations M3 and M8 in the Supplementary Material).

3.5 Hindering the lateral momentum transfer

The six first-neighbors of each chemisorbed H atoms were removed in an orderly fashion, both on the sample and the probe, to explore an extreme situation in which energy transfer along the C-H bonds is made increasingly significant (thus exacerbating any possible effect of the atomic mass of the adsorbate on friction). In these simulations, the lateral transfer of energy between H atoms in the passivation layer should be reduced. At a 0.05 significance level, with the hypothesis that the coefficient of friction is independent of the adsorbate atomic mass, no effect of the atomic mass of the passivation atoms on friction was observed, see Figure 21 and Figure 22.

Figure 21 – Friction force as a function of normal load for sliding in the condition #2 where, for different masses of the chemisorbed atoms (in atomic mass units). The six first-neighbors of each chemisorbed H atom were removed in an orderly fashion. The continuous lines represent linear fits to the data.
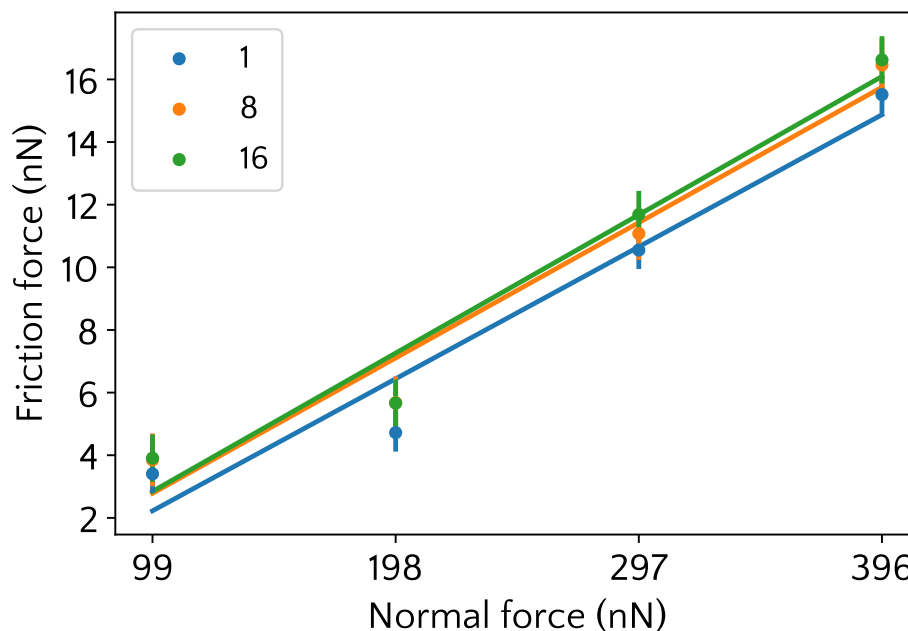
Figure 22 – The coefficient of friction as a function of adsorbate mass for sliding in condition #2. The six first-neighbors of each chemisorbed H atom were removed in an orderly fashion. The continuous lines represent linear fits to the data. Dark and light gray bands are the 1σ and 2σ prediction intervals, respectively. The green line in the inset graph represents the expected behavior for the coefficient of friction according to the approach proposed by Cannara *et al.* [9].
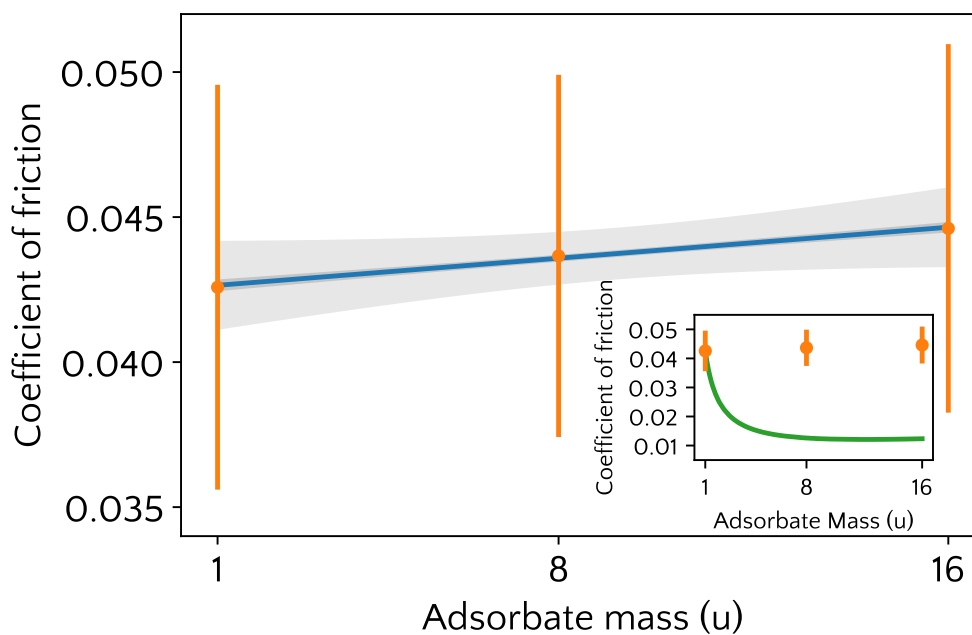
3.6   The effect of changing the surface coverage

An indirect effect of the atomic mass of the passivation atoms on friction, in terms of its effect on surface coverage, has been proposed as a possible reason for the isotopic effect reported by Cannara et al. [9, 19]. Accordingly, we next explore the effect of varying surface coverages of passivating H atoms (mass 1 u) on the friction between probe and sample. Figure 23 shows the friction force between the two diamond surfaces as a function of normal force for different degrees of surface coverage of the sample.

Figure 23 – Friction force as a function of normal load for condition #1 and different surface coverages by H atoms.
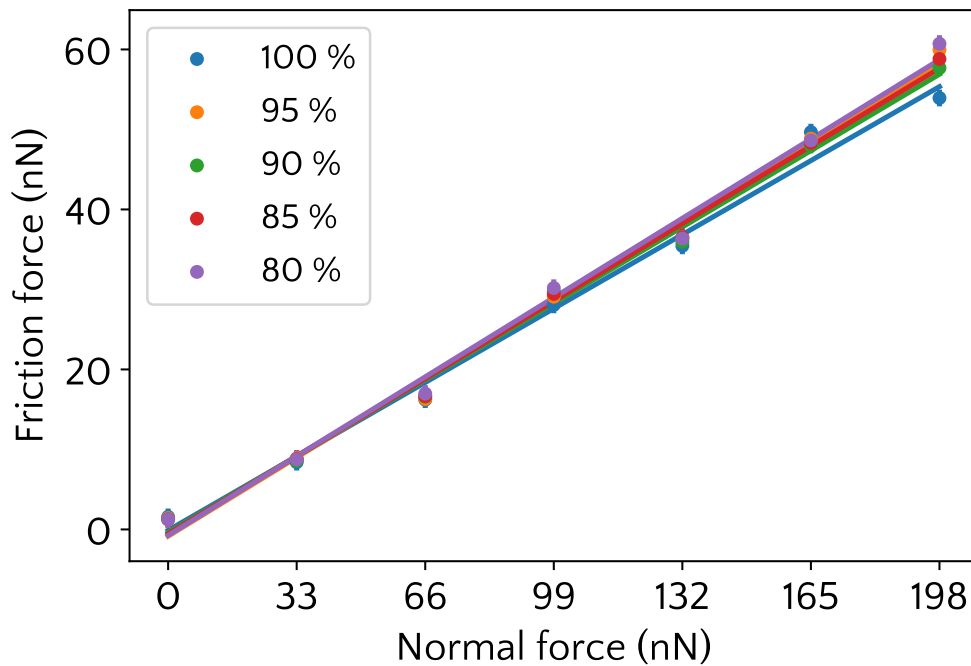
The corresponding coefficients of friction are shown in Figure 24. The slight increase of the coefficient of friction by reducing the surface coverage is much less pronounced than that observed by Mo et al. in their MD simulations of friction for a 80 % surface coverage [19]. In fact, given the estimated uncertainties for the results depicted in Figure 24, we cannot reject the null-slope hypothesis, at a 0.05 significance level, that the coefficient of friction is independent of the surface coverage for sliding in condition #1.

The reasons for the apparent discrepancy between the present results and those of Mo et al. for 80 % surface coverage are not clear but it is possibly related to the form that surface defects were created and whether (and to what degree) the surface was allowed to reconstruct before MD simulations. All simulations here reported were carried out at low temperature (namely, 10 K) and, therefore, surface reconstruction was very much hindered. A few molecular dynamics simulations were performed for the NVT part of the system

coupled to a thermal bath at 300 K, for a 165 nN normal force. Although this temperature is not high enough as to promote any significant surface reconstruction, such tests were performed to reveal any influence of temperature on the previous conclusion. Apart from the already known trend of friction reduction upon temperature increase [36, 85], no difference in friction force was observed when surface coverage was reduced from 100 % to 80 %, even at 300 K.

Figure 24 – The coefficient of friction as a function of surface coverage by H atoms for condition #1. The continuous lines represent linear fits to the data. Dark and light gray bands are the 1σ and 2σ prediction intervals, respectively.
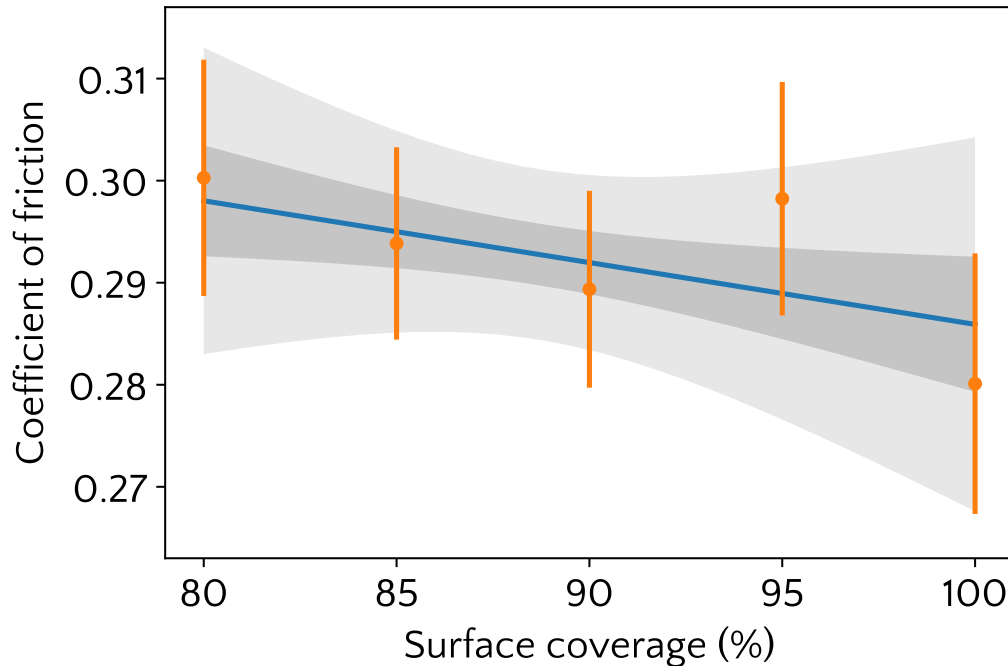
3.7 The effect of carbon dangling bonds on friction

The surface's chemical reactivity influence on friction between probe and sample was explored by substituting up to 20 % of H atoms with carbon, on both the sample and probe. Two main differences between this situation and that simulated for a partially passivated diamond surface is that in the present case, the carbon atoms are disposed of on the outermost atomic layer (i.e., the carbon atoms' dangling bonds are not shielded by the nearest H atoms). Secondly, given that the system is simulated at low temperature, surface reconstruction is highly hindered, and consequently, there are probably three times more dangling bonds available per carbon atom at the outermost layer on the diamond surface, with a significant increase of chemical reactivity.

Figure 25 exhibits the friction force as a function of the percentage of carbon atoms in the passivation layer for a normal force of 33 nN in condition #1. This substitution creates

strongly reactive surfaces by permitting direct bonding between C atoms with dangling bonds on both surfaces (see movie M9 in Supplementary Material). These observations are in good agreement with previous results that reported an increase of friction by replacing hydrogen atoms in the passivation layer with chemically more reactive species, in which case the dynamic formation and rupture of bonds have an important influence friction [36, 86]. Despite the larger estimated uncertainty for the friction force in these simulations, the results suggest that substituting carbon for hydrogen in the passivation layer, at the 2 % level, promotes an increase of friction force similar in magnitude to the isotopic effect reported by Cannara el al, as suggested by Mo el al. This increase of friction force, however, was only observed when both the sample's and counterface's surfaces are chemically reactive which, for the conditions here simulated, only happens in the presence of highly reactive carbon atoms with dangling bonds in the outermost atomic layers.

Figure 25 – Friction force as a function of the percentage of carbon replacing hydrogen in the passivation layers of both sample and counterface's surface for a normal force of 33 nN, in condition #1. The continuous line represents a linear fit to the data.
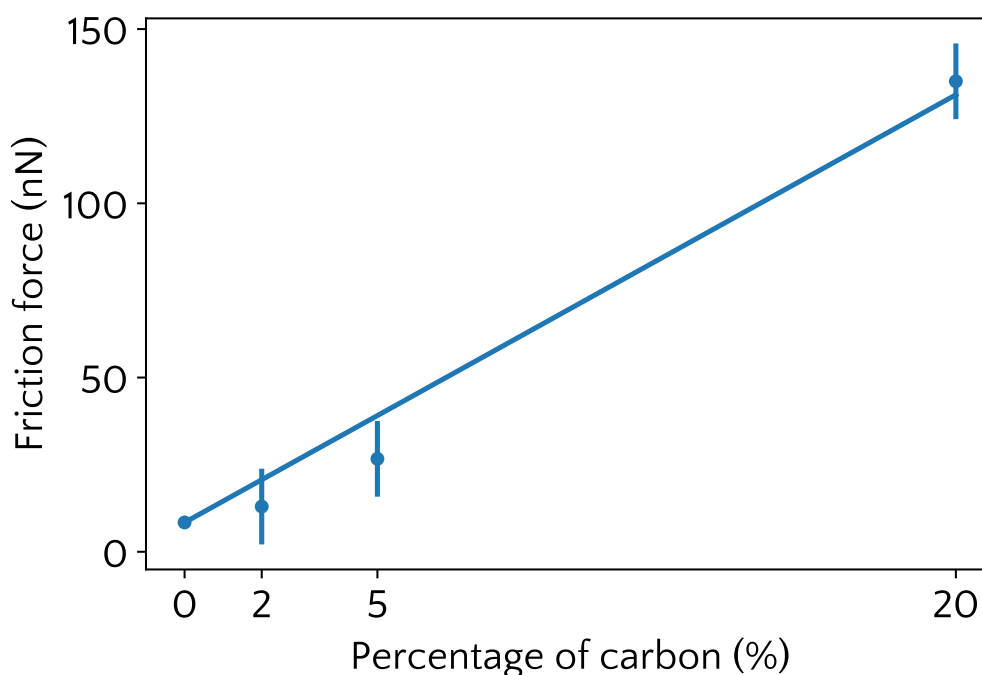
3.8 Data Availability

Supplementary material to this work includes Jupyter notebooks implementing data analysis and several animations illustrating various aspects discussed in the text. For instructions on installing and running Jupyter notebooks see, for instance, <http:

//jupyter.org/>. All data supporting the findings of this study, including input and output files from MD simulations, are available at <https://osf.io/kdb4v/>.

The next chapter will describe the main conclusions obtained in this work.

Part III

Conclusions and Future Works

4 Conclusions

Molecular dynamics simulations of the friction between two H-passivated diamond surfaces revealed no direct effect of the atomic mass of the surface passivation atoms on friction, for two different sliding directions, including a superlubricity condition. The absence of what can be called a direct isotopic effect on the coefficient of friction between diamond surfaces is in good agreement with previous results by Mo et al. [19]. No dependence with the adsorbate atomic mass was observed even in the extreme case where lateral energy transfer between H atoms was virtually eliminated by removal of the neighborhood hydrogens, thus privileging energy (and momentum) transfer along C-H bonds. Modification of the passivation layer, including reduction of surface coverage, only yielded an appreciable effect on the coefficient of friction between the two diamond surfaces when reactive defects were created. This becomes particularly evident when reactive carbon atoms substituted for H in the outermost atomic layers of the sliding surfaces. Accordingly, our MD simulations give support to an indirect isotopic effect on friction (in terms of its influence on surface coverage due to the difference in thermal stability depending on the isotope mass), but only to the extent that defects created in the passivation layer lead to the formation of highly reactive surfaces. However, it must be kept in mind that the same high-temperature thermal treatments that promote the creation of surface defects and, hence, the isotopic effect on friction, may also promote surface reconstruction and lead to chemically non-reactive surfaces, thus inhibiting the very same effect. The isotopic effect on friction may well depend on the balance between these two opposite trends.

The next chapter will present some possibilities of future investigations based on the findings of this work.

5 Future works

Given the difficulty of uncoupling the many dissipation mechanisms that possibly interfere with the friction forces in experimental situations, increasingly sophisticated computer simulations may open new pathways and should be further pursued to isolate and study the different physicochemical contributions that give rise to friction forces. In particular, it remains to be explored to what extent the conclusions of this work (particularly how the difference in thermal stability of H- and D-passivated surfaces, and the creation of reactive surface defects, influence the coefficient of friction) are dependent on the simulation conditions, including normal force and sliding speed.

Bibliography

1 HOLMBERG, K. et al. Global energy consumption due to friction in paper machines. *Tribology International*, v. 62, p. 58–77, 2013. ISSN 0301679X. Cited on page 22.

2 De Mello, S. R. et al. On the phonon dissipation contribution to nanoscale friction by direct contact. *Scientific Reports*, Springer US, v. 7, n. 1, p. 1–8, 2017. ISSN 20452322. Cited on page 22.

3 LISKIEWICZ, T.; BEAKE, B.; SMITH, J. In situ accelerated micro-wear—a new technique to fill the measurement gap. *Surf. Coat. Tech.*, Elsevier, v. 205, n. 5, p. 1455–1459, 2010. Cited on page 22.

4 HUTCHINGS, I. M. Leonardo da vinci s studies of friction. *Wear*, Elsevier, v. 360, p. 51–66, 2016. Cited 3 times on pages 22, 26, and 27.

5 POPOVA, E.; POPOV, V. L. The research works of coulomb and amontons and generalized laws of friction. *Friction*, Springer, v. 3, n. 2, p. 183–190, 2015. Cited on page 22.

6 MATE, C. M. *Tribology on the Small Scale*. Oxford University Press, 2007. ISBN 9780198526780. Available from Internet: <http://www.oxfordscholarship.com/view/10.1093/acprof:oso/9780198526780.001.0001/acprof-9780198526780>. Cited 8 times on pages 8, 22, 27, 28, 29, 30, 31, and 32.

7 MO, Y.; TURNER, K. T.; SZLUFARSKA, I. Friction laws at the nanoscale. *Nature*, Nature Publishing Group, v. 457, n. 7233, p. 1116–1119, 2009. Cited on page 22.

8 KRIM, J.; WIDOM, A. Damping of a crystal oscillator by an adsorbed monolayer and its relation to interfacial viscosity. *Physical Review B*, APS, v. 38, n. 17, p. 12184, 1988. Cited on page 22.

9 CANNARA, R. J. et al. Nanoscale Friction Varied by Isotopic Shifting of Surface Vibrational Frequencies. *Science*, v. 318, n. November, p. 780–783, 2007. Cited 10 times on pages 9, 10, 22, 23, 38, 46, 60, 61, 62, and 63.

10 TOCHA, E.; SCHÖNHERR, H.; Julius Vancso, G. Quantitative nanotribology by AFM: A novel universal calibration platform. *Langmuir*, v. 22, n. 5, p. 2340–2350, 2006. ISSN 07437463. Cited on page 22.

11 CARPICK, R. W.; SALMERON, M. Scratching the surface: fundamental investigations of tribology with atomic force microscopy. *Chemical reviews*, ACS Publications, v. 97, n. 4, p. 1163–1194, 1997. Cited on page 22.

12 BERMAN, D.; ERDEMIR, A.; SUMANT, A. V. Approaches for achieving superlubricity in two-dimensional materials. *ACS nano*, ACS Publications, v. 12, n. 3, p. 2122–2137, 2018. Cited on page 22.

13 BRUKMAN, M. J. et al. Temperature dependence of single-asperity diamond-diamond friction elucidated using AFM and MD simulations. *Journal of Physical Chemistry C*, v. 112, n. 25, p. 9358–9369, 2008. ISSN 19327447. Cited 2 times on pages 22 and 41.

14   GAO, G. et al. Atomic-scale friction on diamond: A comparison of different sliding directions on (001) and (111) surfaces using MD and AFM. *Langmuir*, v. 23, n. 10, p. 5394–5405, 2007. ISSN 07437463.   Cited 4 times on pages 22, 41, 58, and 60.

15   LI, Q. et al. Speed dependence of atomic stick-slip friction in optimally matched experiments and molecular dynamics simulations. *Physical Review Letters*, v. 106, n. 12, p. 1–4, 2011. ISSN 00319007.   Cited 2 times on pages 22 and 50.

16   Van Den Oetelaar, R. J.; FLIPSE, C. F. Atomic-scale friction on diamond(111) studied by ultra-high vacuum atomic force microscopy. *Surface Science*, v. 384, n. 1-3, 1997. ISSN 00396028.   Cited on page 22.

17   PERSSON, B. N. J. *Sliding Friction*. Berlin, Heidelberg: Springer Berlin Heidelberg, 2000. v. 26. 367 p. (NanoScience and Technology, v. 26). ISBN 978-3-642-08652-6. Available from Internet: <http://link.springer.com/10.1007/978-3-662-02882-7http://link.springer.com/10.1007/978-3-662-04283-0>.   Cited 9 times on pages 8, 23, 32, 33, 34, 35, 36, 37, and 38.

18   PERSSON, B. N. et al. Low-frequency adsorbate vibrational relaxation and sliding friction. *Physical Review B - Condensed Matter and Materials Physics*, v. 59, n. 18, p. 11777–11791, 1999. ISSN 1550235X.   Cited 4 times on pages 23, 34, 35, and 36.

19   MO, Y.; MÜSER, M. H.; SZLUFARSKA, I. Origin of the isotope effect on solid friction. *Physical Review B - Condensed Matter and Materials Physics*, v. 80, n. 15, p. 1–7, 2009. ISSN 10980121.   Cited 10 times on pages 23, 38, 39, 41, 46, 57, 58, 60, 63, and 68.

20   LARSEN, F. H. *Molecular Dynamics modeling of single asperity contact*. 2017.   Cited 8 times on pages 8, 26, 39, 40, 42, 43, 44, and 45.

21   HUTCHINGS, I.; SHIPWAY, P. *Tribology: friction and wear of engineering materials*. 2. ed. [S.l.]: Butterworth-Heinemann, 2017. 412 p. ISBN 9780081009109.   Cited on page 27.

22   BHUSHAN, B. *Introduction to Tribology*. The Atrium, Southern Gate, Chichester, West Sussex, PO19 8SQ, UK: John Wiley Sons, Ltd, 2013. v. 17. 2–5 p. ISBN 9781118403259. Available from Internet: <http://doi.wiley.com/10.1002/9781118403259>. Cited 4 times on pages 8, 27, 28, and 29.

23   BOWDEN, D. T. F. P. *The friction and lubrication of solids*. [S.l.]: Oxford, Clarendon Press, 1950. ISBN 9780198507772.   Cited on page 29.

24   TABOR, D. The role of surface and intermolecular forces in thin film lubrication. In: GEORGES, J. (Ed.). *Microscopic Aspects of Adhesion and Lubrication*. Elsevier, 1981, (Tribology Series, v. 7). p. 651 – 682. Available from Internet: <http://www.sciencedirect.com/science/article/pii/S0167892208709131>.   Cited on page 29.

25   HOMOLA, A. M. et al. Fundamental experimental studies in tribology: The transition from "interfacial" friction of undamaged molecularly smooth surfaces to "normal" friction with wear. *Wear*, v. 136, n. 1, p. 65–83, feb 1990. ISSN 00431648. Available from Internet: <https://linkinghub.elsevier.com/retrieve/pii/004316489090072I>.   Cited on page 29.

26 BERMAN, A.; DRUMMOND, C.; ISRAELACHVILI, J. Amontons' law at the molecular level. *Tribology Letters*, v. 4, n. 2, p. 95–101, 1998. ISSN 10238883. Cited 2 times on pages 8 and 30.

27 GEE, M. L. et al. Liquid to solidlike transitions of molecularly thin films under shear. *The Journal of Chemical Physics*, v. 93, n. 3, p. 1895–1906, 1990. ISSN 00219606. Cited on page 30.

28 GAO, J. et al. Frictional forces and Amontons' law: From the molecular to the macroscopic scale. *Journal of Physical Chemistry B*, v. 108, n. 11, p. 3410–3425, 2004. ISSN 15206106. Cited 2 times on pages 30 and 60.

29 ISRAELACHVILI, J. N. Importance of picoScale topography of surfaces for adhesion, friction, and failure. *MRS Bulletin*, v. 30, n. 7, p. 533–539, 2005. ISSN 08837694. Cited on page 30.

30 PERSSON, B. N.; RYBERG, R. Brownian motion and vibrational phase relaxation at surfaces: CO on Ni(111). *Physical Review B*, v. 32, n. 6, p. 3586–3596, 1985. ISSN 01631829. Cited on page 35.

31 HALL, B.; MILLS, D. L.; BLACK, J. E. Lattice dynamics of rare-gas overlayers on smooth surfaces. *Physical Review B*, v. 32, n. 8, p. 4932–4945, oct 1985. ISSN 0163-1829. Available from Internet: <https://link.aps.org/doi/10.1103/PhysRevB.32.4932>. Cited on page 36.

32 LEWIS, S. P. et al. Continuum elastic theory of adsorbate vibrational relaxation. *Journal of Chemical Physics*, v. 108, n. 3, p. 1157–1161, 1998. ISSN 00219606. Cited on page 36.

33 BRUCH, L.; HANSEN, F. Mode damping in a commensurate monolayer solid. *Physical Review B - Condensed Matter and Materials Physics*, v. 55, n. 3, p. 1782–1792, 1997. ISSN 1550235X. Cited on page 36.

34 SINNOTT, S. B. et al. Computer Simulations of Nanometer-Scale Indentation and Friction. In: BHUSHAN, B. (Ed.). *Nanotribology and Nanomechanics.* Cham: Springer International Publishing, 2017. p. 301–370. Available from Internet: <http://link.springer.com/10.1007/978-3-319-51433-8{_}7http://link.springer.com/10.1007/978-3-319-51433->. Cited 2 times on pages 39 and 48.

35 RAPAPORT, D. C. *The Art of Molecular Dynamics Simulation.* Cambridge University Press, 2004. 400 p. ISBN 9780521825689. Available from Internet: <https://www.cambridge.org/core/product/identifier/9780511816581/type/book>. Cited on page 39.

36 DONG, Y.; LI, Q.; MARTINI, A. Molecular dynamics simulation of atomic friction: A review and guide. *Journal of Vacuum Science & Technology A: Vacuum, Surfaces, and Films*, v. 31, n. 3, p. 030801, 2013. ISSN 0734-2101. Cited 7 times on pages 39, 40, 48, 50, 51, 64, and 65.

37 SENIOR, E. On the determination of molecular fields. —II. From the equation of state of a gas. *Proceedings of the Royal Society of London. Series A, Containing Papers of a Mathematical and Physical Character*, v. 106, n. 738, p. 463–477, oct 1924. ISSN 0950-1207.

Available from Internet: <https://royalsocietypublishing.org/doi/10.1098/rspa.1924.0082>.
Cited on page 39.

38 DAW, M. S.; BASKES, M. I. Embedded-atom method: Derivation and
application to impurities, surfaces, and other defects in metals. *Physical Review
B*, v. 29, n. 12, p. 6443–6453, jun 1984. ISSN 0163-1829. Available from Internet:
<https://link.aps.org/doi/10.1103/PhysRevB.29.6443>. Cited on page 40.

39 FOILES, S. M.; BASKES, M. I.; DAW, M. S. Embedded-atom-method functions
for the fcc metals Cu, Ag, Au, Ni, Pd, Pt, and their alloys. *Physical Review B*,
v. 33, n. 12, p. 7983–7991, jun 1986. ISSN 0163-1829. Available from Internet:
<https://link.aps.org/doi/10.1103/PhysRevB.33.7983>. Cited on page 40.

40 STILLINGER, F. H.; WEBER, T. A. Computer simulation of local order in condensed
phases of silicon. *Physical Review B*, v. 31, n. 8, p. 5262–5271, apr 1985. ISSN 0163-1829.
Available from Internet: <https://link.aps.org/doi/10.1103/PhysRevB.31.5262>. Cited
on page 40.

41 TERSOFF, J. New empirical model for the structural properties of silicon.
Physical Review Letters, v. 56, n. 6, p. 632–635, feb 1986. ISSN 0031-9007.
Available from Internet: <https://link.aps.org/doi/10.1103/PhysRevB.37.6991https:
//link.aps.org/doi/10.1103/PhysRevLett.56.632>. Cited on page 40.

42 TERSOFF, J. Empirical Interatomic Potential for Carbon, with Applications to
Amorphous Carbon. *Physical Review Letters*, v. 61, n. 25, p. 2879–2882, dec 1988. ISSN
0031-9007. Available from Internet: <https://link.aps.org/doi/10.1103/PhysRevLett.61.
2879>. Cited on page 40.

43 TERSOFF, J. New empirical approach for the structure and energy of covalent
systems. *Physical Review B*, v. 37, n. 12, p. 6991–7000, apr 1988. ISSN 0163-1829.
Available from Internet: <https://link.aps.org/doi/10.1103/PhysRevB.37.6991>. Cited
on page 40.

44 TOMAS, C. de; SUAREZ-MARTINEZ, I.; MARKS, N. A. Graphitization
of amorphous carbons: A comparative study of interatomic potentials. *Carbon*,
v. 109, p. 681–693, nov 2016. ISSN 00086223. Available from Internet: <https:
//linkinghub.elsevier.com/retrieve/pii/S0008622316306790>. Cited 2 times on pages 40
and 41.

45 BRENNER, D. W. Empirical potential for hydrocarbons for use in simulating the
chemical vapor deposition of diamond films. *Physical Review B*, v. 42, n. 15, p. 9458–9471,
1990. ISSN 01631829. Cited 2 times on pages 40 and 41.

46 BRENNER, D. W. et al. A second-generation reactive empirical bond order (REBO)
potential energy expression for hydrocarbons. *Journal of Physics Condensed Matter*, v. 14,
n. 4, p. 783–802, 2002. ISSN 09538984. Cited on page 40.

47 STUART, S. J.; TUTEIN, A. B.; HARRISON, J. A. A reactive potential for
hydrocarbons with intermolecular interactions. *Journal of Chemical Physics*, v. 112, n. 14,
p. 6472–6486, 2000. ISSN 00219606. Cited 4 times on pages 40, 41, 42, and 46.

48   Van Duin, A. C. et al. ReaxFF: A reactive force field for hydrocarbons. *Journal of Physical Chemistry A*, v. 105, n. 41, p. 9396–9409, 2001. ISSN 10895639.   Cited on page 40.

49   Goverapet Srinivasan, S.; Van Duin, A. C.; GANESH, P. Development of a ReaxFF potential for carbon condensed phases and its application to the thermal fragmentation of a large fullerene. *Journal of Physical Chemistry A*, v. 119, n. 4, p. 571–580, 2015. ISSN 15205215.   Cited on page 41.

50   LIANG, T. et al. Classical atomistic simulations of surfaces and heterogeneous interfaces with the charge-optimized many body (COMB) potentials. *Materials Science and Engineering R: Reports*, Elsevier B.V., v. 74, n. 9, p. 255–279, 2013. ISSN 0927796X. Available from Internet: <http://dx.doi.org/10.1016/j.mser.2013.07.001>.   Cited on page 41.

51   PLIMPTON, S. J.; THOMPSON, A. P. Computational aspects of many-body potentials. *MRS Bulletin*, v. 37, n. 5, p. 513–521, 2012. ISSN 08837694.   Cited on page 41.

52   LOS, J. H.; FASOLINO, A. Intrinsic long-range bond-order potential for carbon: Performance in monte carlo simulations of graphitization. *Phys. Rev. B*, American Physical Society, v. 68, p. 024107, Jul 2003. Available from Internet: <https://link.aps.org/doi/10.1103/PhysRevB.68.024107>.   Cited on page 41.

53   LOS, J. H. et al. Improved long-range reactive bond-order potential for carbon. i. construction. *Phys. Rev. B*, American Physical Society, v. 72, p. 214102, Dec 2005. Available from Internet: <https://link.aps.org/doi/10.1103/PhysRevB.72.214102>.   Cited on page 41.

54   GHIRINGHELLI, L. M. et al. Improved long-range reactive bond-order potential for carbon. ii. molecular simulation of liquid carbon. *Phys. Rev. B*, American Physical Society, v. 72, p. 214103, Dec 2005. Available from Internet: <https://link.aps.org/doi/10.1103/PhysRevB.72.214103>.   Cited on page 41.

55   MARKS, N. A. Generalizing the environment-dependent interaction potential for carbon. *Phys. Rev. B*, American Physical Society, v. 63, p. 035401, Dec 2000. Available from Internet: <https://link.aps.org/doi/10.1103/PhysRevB.63.035401>.   Cited on page 41.

56   MARKS, N. Modelling diamond-like carbon with the environment-dependent interaction potential. *Journal of Physics Condensed Matter*, v. 14, n. 11, p. 2901–2927, 2002. ISSN 09538984.   Cited on page 41.

57   LIU, J. et al. Vacancy-controlled friction on 2D materials: Roughness, flexibility, and chemical reaction. *Carbon*, v. 142, n. October, p. 363–372, 2019. ISSN 00086223.   Cited on page 41.

58   BEN, J. *Expansão Térmica de Redes Aleatórias de Carbono Expansão Térmica de Redes Aleatórias de Carbono*. 2017.   Cited 2 times on pages 41 and 42.

59   DIAS, R. A. *Atrito em escala nanométrica Um estudo por simulação*. Thesis (Doctorate), 2007.   Cited on page 42.

60 RAPAPORT, D. C. *The Art of Molecular Dynamics Simulation*. Cambridge University Press, 2004. 400 p. ISBN 9780521825689. Available from Internet: <https://www.cambridge.org/core/product/identifier/9780511816581/type/book>. Cited 4 times on pages 8, 42, 43, and 44.

61 FRENKEL, D.; SMIT, B.; RATNER, M. A. Understanding Molecular Simulation: From Algorithms to Applications. *Physics Today*, v. 50, n. 7, p. 66–66, jul 1997. ISSN 0031-9228. Available from Internet: <http://physicstoday.scitation.org/doi/10.1063/1.881812>. Cited 2 times on pages 44 and 45.

62 De Miguel, E.; JACKSON, G. The nature of the calculation of the pressure in molecular simulations of continuous models from volume perturbations. *Journal of Chemical Physics*, v. 125, n. 16, p. 1–11, 2006. ISSN 00219606. Cited on page 44.

63 BERENDSEN, H. J. et al. Molecular dynamics with coupling to an external bath. *The Journal of Chemical Physics*, v. 81, n. 8, p. 3684–3690, 1984. ISSN 00219606. Cited on page 45.

64 ANDERSEN, H. C. Molecular dynamics simulations at constant pressure and/or temperature. *The Journal of Chemical Physics*, v. 72, n. 4, p. 2384–2393, 1980. ISSN 00219606. Cited on page 45.

65 NOSÉ, S. A unified formulation of the constant temperature molecular dynamics methods. *The Journal of Chemical Physics*, v. 81, n. 1, p. 511–519, 1984. ISSN 00219606. Cited on page 45.

66 HOOVER, W. G. Canonical dynamics: Equilibrium phase-space distributions. *Physical Review A*, v. 31, n. 3, p. 1695–1697, mar 1985. ISSN 0556-2791. Available from Internet: <https://link.aps.org/doi/10.1103/PhysRevA.31.1695>. Cited on page 45.

67 HOOVER, W. G. Constant-pressure equations of motion. *Physical Review A*, v. 34, n. 3, p. 2499–2500, sep 1986. ISSN 0556-2791. Available from Internet: <https://link.aps.org/doi/10.1103/PhysRevA.34.2499>. Cited on page 45.

68 PLIMPTON, S. Fast Parallel AlgorithmsforShort–Range Molecular Dynamics. *Journal of Computational Physics*, v. 117, p. 1–19, 1995. ISSN 00219991. Available from Internet: <http://www.cs.sandia.gov/\protect\begingroup\immediate\write\@unused\def\MessageBreak˙\let\protect\edefYoumayprovideadefinitionwith\MessageBreak\DeclareUnicodeCharacter\errhelp\let\def\MessageBreak˙(inputenc)\def\errmessagePackageinputencError: UnicodecharacterâĹij(U+223C)\MessageBreaknotsetupforusewithLaTeX. ¨Seetheinputencpackagedocumentationforexplanation.¨TypeH<return> forimmediatehelp\endgroupsjplimp/main.html>. Cited on page 46.

69 STUKOWSKI, A. Visualization and analysis of atomistic simulation data with OVITO–the open visualization tool. *Modelling and Simulation in Materials Science and Engineering*, IOP Publishing, v. 18, n. 1, p. 015012, dec 2009. Available from Internet: <https://doi.org/10.1088%2F0965-0393%2F18%2F1%2F015012>. Cited on page 47.

70 SHIMIZU, J. et al. Molecular dynamics simulation of friction on the atomic scale. *Nanotechnology*, v. 9, n. 2, p. 118–123, 1998. ISSN 09574484. Cited on page 50.

71 HIRANO, M.; SHINJO, K. Atomistic locking and friction. *Physical Review B*, APS, v. 41, n. 17, p. 11837, 1990.   Cited on page 51.

72 BREHM, M.; KIRCHNER, B. TRAVIS - A free analyzer and visualizer for monte carlo and molecular dynamics trajectories. *Journal of Chemical Information and Modeling*, v. 51, n. 8, p. 2007–2023, 2011. ISSN 15499596.   Cited on page 52.

73 THOMAS, M. et al. Simulating the vibrational spectra of ionic liquid systems: 1-Ethyl-3-methylimidazolium acetate and its mixtures. *The Journal of Chemical Physics*, v. 141, n. 2, p. 024510, jul 2014. ISSN 0021-9606. Available from Internet: <http://dx.doi.org/10.1063/1.4887082http://aip.scitation.org/doi/10.1063/1.4887082>. Cited on page 52.

74 BREHM, M. et al. TRAVIS—A free analyzer for trajectories from molecular simulation. *Journal of Chemical Physics*, AIP Publishing, LLC, v. 152, n. 16, 2020. ISSN 10897690. Available from Internet: <https://doi.org/10.1063/5.0005078>.   Cited on page 52.

75 KLUYVER, T. et al. Jupyter notebooks - a publishing format for reproducible computational workflows. In: *Positioning and Power in Academic Publishing: Players, Agents and Agendas*. [S.l.: s.n.], 2016. p. 87–90.   Cited on page 53.

76 SHEN, H. Interactive Notebooks: Sharing the Code. *Nature*, v. 515, p. 151–152, 2014. Cited on page 53.

77 NEWVILLE, M. et al. *lmfit/lmfit-py 1.0.1*. Zenodo, 2020. Available from Internet: <https://doi.org/10.5281/zenodo.3814709>.   Cited on page 53.

78 LEBIGOT, E. O. *Uncertainties: a Python package for calculations with uncertainties*. 2020. Available from Internet: <https://uncertainties-python-package.readthedocs.io/en/latest/>.   Cited on page 53.

79 JENSEN, J. O. Vibrational frequencies and structural determination of adamantane. *Spectrochimica Acta - Part A: Molecular and Biomolecular Spectroscopy*, v. 60, n. 8-9, p. 1895–1905, 2004. ISSN 13861425.   Cited on page 55.

80 BRELA, M. Z. et al. Molecular Dynamics Simulations of Vibrational Spectra of Hydrogen-Bonded Systems. *Frontiers of Quantum Chemistry*, p. 353–376, 2018.   Cited on page 55.

81 HIRANO, M.; SHINJO, K. Superlubricity and frictional anisotropy. *Wear*, v. 168, n. 1-2, p. 121–125, 1993. ISSN 00431648.   Cited on page 56.

82 DONG, Y. et al. Friction evolution with transition from commensurate to incommensurate contacts between graphene layers. *Tribology International*, Elsevier Ltd, v. 136, n. March, p. 259–266, 2019. ISSN 0301679X. Available from Internet: <https://doi.org/10.1016/j.triboint.2019.03.058>.   Cited 2 times on pages 56 and 60.

83 GAO, G. T.; MIKULSKI, P. T.; HARRISON, J. A. Molecular-scale tribology of amorphous carbon coatings: Effects of film thickness, adhesion, and long-range interactions. *Journal of the American Chemical Society*, v. 124, n. 24, p. 7202–7209, 2002. ISSN 00027863.   Cited on page 57.

84   HARRISON, J. A. et al. Atomistic simulations of friction at sliding diamond interfaces. *MRS Bulletin*, v. 18, n. 5, p. 50–53, 1993. ISSN 19381425.   Cited on page 60.

85   JANSEN, L. et al. Temperature dependence of atomic-scale stick-slip friction. *Phys. Rev. Lett.*, American Physical Society, v. 104, p. 256101, Jun 2010. Available from Internet: <https://link.aps.org/doi/10.1103/PhysRevLett.104.256101>.   Cited on page 64.

86   DAG, S.; CIRACI, S. Atomic scale study of superlow friction between hydrogenated diamond surfaces. *Physical Review B*, APS, v. 70, n. 24, p. 241401, 2004.   Cited on page 65.

Appendix

APPENDIX A – Lammps metals units

- mass = grams/mole;

- distance = Angstroms;

- time = picoseconds;

- energy = eV;

- velocity = Angstroms/picosecond;

- force = eV/Angstrom;

- torque = eV;

- temperature = Kelvin;

- pressure = bars;

- dynamic viscosity = Poise;

- charge = multiple of electron charge (1.0 is a proton);

- dipole = charge*Angstroms;

- electric field = volts/Angstrom;

- density = gram/cm-dim.

APPENDIX B – Build slab script

```
 1 # ----------------------- INITIALIZATION --------------------------
 2 echo screen
 3 units           metal
 4 dimension       3
 5 boundary        p p m
 6 atom_style      atomic
 7 variable latparam equal 3.57
 8
 9 #orthogonal vectors repetitions in each direction
10 variable Nx equal 28
11 variable Ny equal 27
12 variable Nz equal 3
13
14 #box simulation dimensions
15 variable box_x equal ${Nx}*sqrt(2)*${latparam}
16 variable box_y equal ${Ny}*(3/2)*${latparam}
17 variable box_z equal ${Nz}*sqrt(3)*${latparam}
18
19 #box simulation limits
20 variable min_z equal -${box_z}-0.8
21 variable max_z equal 1.6
22 variable max_x equal ${box_x}/2.0
23 variable min_x equal -${max_x}
24 variable max_y equal ${box_y}/2.0-0.95
25 variable min_y equal -${box_y}/2.0-0.95
26
27 #box simulation creation
28 region simul_box block ${min_x} ${max_x} ${min_y} ${max_y} ${min_z} ${
     max_z}
29 create_box      3 simul_box
30
31 # ----------------------- ATOM DEFINITION --------------------------
32 lattice         diamond ${latparam} orient x 1 -1 0 orient y 1 1 -2
     orient z 1 1 1
33 create_atoms    1 box
34
35 mass 1 12.0107
36 mass 2 1.01
37 mass 3 12.0107
38
39 #define hydrogens
40 region top_slabHR block INF INF INF INF 1.4 1.6 units box
41 group top_slabHG region top_slabHR
```

```
42 set group top_slabHG type 2
43
44 #define rigid carbons on the base
45 region fixoR block INF INF INF INF INF -18.0 units box
46 group fixoG region fixoR
47 set group fixoG type 3
48
49 # ------------------------ FORCE FIELDS ----------------------------
50 pair_style      airebo 3 1 0
51 pair_coeff      * * /opt/lammps/potentials/CH.airebo C H C
52
53 timestep 0.0002
54 dump     1 all custom 100 dump.teste.* id type xs ys zs fx fy fz vx vy vz
55
56 run 1
57 quit
```

APPENDIX C — Build tip script

```
 1 # ---------------------- INITIALIZATION --------------------------
 2 echo screen
 3 units      metal
 4 dimension 3
 5 boundary   m m m
 6 atom_style  atomic
 7 variable latparam equal 3.57
 8
 9 #orthogonal vectors repetitions in each direction
10 variable Nx equal 4
11 variable Ny equal 4
12 variable Nz equal 3
13
14 #box simulation dimensions
15 variable box_x equal ${Nx}*sqrt(2)*${latparam}
16 variable box_y equal ${Ny}*(3/2)*${latparam}
17 variable box_z equal ${Nz}*sqrt(3)*${latparam}
18
19 #box simulation limits
20 variable min_z equal 2.2
21 variable max_z equal ${box_z}+2.2
22 variable max_x equal ${box_x}/2.0+3.0
23 variable min_x equal -${max_x}
24 variable max_y equal ${box_y}/2.0+2.5
25 variable min_y equal -${max_y}
26
27 #box simulation creation
28 region simul_box block ${min_x} ${max_x} ${min_y} ${max_y} ${min_z} ${
      max_z}
29 create_box  2 simul_box
30
31 # --------------------- ATOM DEFINITION --------------------------
32 lattice    diamond ${latparam} orient x 1 -1 0 orient y 1 1 -2 orient z 1
       1 1
33 create_atoms  1 box
34
35 mass 1 12.0107
36 mass 2 1.01
37
38 # ---------------------- FORCE FIELDS ---------------------------
39 pair_style  airebo 3 1 0
40 pair_coeff  * * /opt/lammps/potentials/CH.airebo C H
41
```

```
42 timestep 0.0001
43 dump     1 all custom 1 dump.bloco.* id type xs ys zs fx fy fz vx vy vz
44
45 run 1
```

APPENDIX D – The main script

```
 1 echo screen
 2 dimension 3
 3 boundary   p p m
 4 atom_style       atomic
 5 neighbor         2.0 bin
 6 units metal
 7 neigh_modify     delay 5
 8
 9 #####################################################################
10 ###### DEFINING THE SIMULATION CONDITIONS
11 #####################################################################
12
13 variable T equal 10.0
14 variable P_normal_bar equal 600000.0
15 variable area_top_block equal 662.2509
16 variable N_atoms_press equal 263
17 variable F_normal equal -${area_top_block}*${P_normal_bar}*6.242E-7/${
     N_atoms_press} #area*press*press_conversion/N_atoms
18 variable log_file_name string "thermo_output.txt"
19 variable separation equal 1.7
20 variable rotation_angle equal 15.0
21
22 #####################################################################
23 ##### IMPORTING STRUCTURES
24 #####################################################################
25
26 #Importing the slab and aligning its top with the z = 0 plane
27 read_data hydrogenated_slab.dat
28 displace_atoms all move 0.0 0.0 -1.54586
29
30 #Adding the tip a little bit outside of the center of the slab,
     positioning the base according to a pre-established distance of the
     surface. The distance is specified by the variable {separation}, in
     angstroms
31 variable shift_block equal -1.0
32 read_data hydrogenated_block.dat add append shift 0.0 0.0 ${shift_block}
33
34 #####################################################################
35 ##### ATOM DEFINITIONS AND POTENTIAL
36 #####################################################################
37
38 pair_style       airebo 3.0 1 0
39 pair_coeff * * /path_to_the_lammps_folder/lammps/potentials/CH.airebo C
```

```
      H C C
40
41 mass 1 12.0107 # not fixed carbons
42 mass 2 1.00784 # hydrogens
43 mass 3 12.0107 # carbons of the slab fixed region
44 mass 4 12.0107 # carbons of the tip fixed region
45
46 #####################################################################
47 ##### GROUP DEFINITIONS
48 #####################################################################
49
50 #slab
51 group fixoG type 3 #fixed region of the slab
52
53 #probe block
54 region blockR block INF INF INF INF 0.5 INF units box
55 group blockG region blockR
56
57 #superior layer of the tip
58 region top_blockR block INF INF INF INF 18 INF
59 group top_blockG region top_blockR
60
61 #removing hydrogens of the top of the tip
62 group hidrogeniosG type 2
63 group hidrogenios_topG intersect hidrogeniosG top_blockG
64 delete_atoms group hidrogenios_topG
65
66 #define the top of the tip with a different kind of atom (better
      visualisation on Ovito)
67 set group top_blockG type 4
68
69 #define group of atoms participating of the dynamic (not fixed)
70 region nveblocoR block INF INF INF INF 0.5 10.0 units box
71 group nveblocoG region nveblocoR
72
73 region nvtblocoR block INF INF INF INF 10.1 18.0 units box
74 group nvtblocoG region nvtblocoR
75
76 region nveslabR block INF INF INF INF -9 0.01 units box
77 group nveslabG region nveslabR
78
79 region nvtslabR block INF INF INF INF -19 -8.9 units box
80 group nvtslabG region nvtslabR
81
82 group dinamicoG union nveblocoG nvtblocoG nveslabG nvtslabG
83
84
```

```
85  ############################################################################
86  ##### OUTPUT CONTROL
87  ############################################################################
88
89  #the reduce command adds the values in the vector to a global total
90  compute forcex_block blockG reduce sum fx
91  compute forcey_block blockG reduce sum fy
92  compute forcez_block blockG reduce sum fz
93  compute forcex_top top_blockG reduce sum fx
94  compute forcey_top top_blockG reduce sum fy
95  compute forcez_top top_blockG reduce sum fz
96  compute kinetic_energy_per_atom all ke/atom
97
98  # calculates the center of mass of the group of atoms, including all
         effects due to atoms that pass periodic limits
99  compute comBloco blockG com
100
101 #adds the values in the vector to a global total and then divides by the
         number of values    in    the vector
102 compute ave_forcex_block blockG reduce ave fx
103 compute ave_forcey_block blockG reduce ave fy
104 compute ave_forcez_block blockG reduce ave fz
105
106 #calculates the temperature of a group of atoms after subtracting the
         velocity of the center of mass of the group
107 compute temp_dinamico dinamicoG temp/com
108
109 #overwrites the temperature calculation pattern by the format defined in
         the compute command
110 thermo_modify temp temp_dinamico
111
112 #write system informations every 200 steps
113 thermo 200
114 thermo_style custom step pe temp c_comBloco[1] c_comBloco[2] c_comBloco
         [3] c_forcex_block c_forcey_block c_forcez_block c_forcez_top
115
116 #dump file for visualization
117 dump    1 all custom 500 dump.nosehoover.* id type xs ys zs fx fy fz vx
         vy vz c_kinetic_energy_per_atom
118
119 ############################################################################
120 ##### GENERATING SIMPLE OUTPUT FILE
121 ############################################################################
122
123 #timestep
124 variable        print_step equal "step"
125
```

```
126 #temperature of the group dinamicoG
127 variable        print_temp equal "temp"
128
129 #spring forces
130 #the spring properties are set to zero before the spring is created
131 variable        spring_fx   equal 0.0
132 variable        spring_fy   equal 0.0
133 variable        spring_fz   equal 0.0
134 variable        spring_ftot   equal 0.0
135
136 #center of mass coordinate of the tip
137 variable        COMy_block      equal c_comBloco[2]
138
139 #average force on the tip
140 variable        fx_block_ave     equal c_ave_forcex_block
141 variable        fy_block_ave     equal c_ave_forcey_block
142 variable        fz_block_ave     equal c_ave_forcez_block
143
144 #center of mass in z of the  g r o u   top_blockG
145 variable        COMz_top        equal xcm(top_blockG,z)
146
147 #total potential energy
148 variable        potential_energy   equal   pe
149
150 #write the values of the variables defined
151 fix fixprintID all print 200 "${print_step} ${potential_energy} ${
    print_temp} ${spring_fy} ${spring_ftot} ${COMy_block} ${fz_block_ave}
     ${COMz_top}" file ${log_file_name} screen no title "Step PE(eV)
    Temperature(K) Fy_spring(eV\A)  Ftotal_spring(eV\A) COMy_block(A)
    fz_block_ave COMz_top"
152
153 ##########################################################################
154 ##### TIP ALIGNMENT
155 ##########################################################################
156
157 #tip rotation around its center of mass, the rotation axis pass exactly
    by one hydrogen atoms of the base
158 displace_atoms blockG rotate 12.6111 13.106 0.0 0 0 1 ${rotation_angle}
159
160 ##########################################################################
161 ##### ENERGY MINIMIZATION
162 ##########################################################################
163
164 #minimization of the tip away from surface
165 displace_atoms blockG move 0.0 0.0 8.0
166 minimize 1.0e-4 1.0e-4 100000 100000
167
```

```
168 #moves the tip closer leaving a tip/slab space defined in the variables
        and then realize a new minimization
169 displace_atoms blockG move 0.0 0.0 -8.0
170 minimize 1.0e-4 1.0e-4 100000 100000
171
172 #######################################################################
173 #### FIXES
174 #######################################################################
175
176 #superior layer of the tip as a rigid block
177 fix rigidBlockID top_blockG rigid single force 1 off on on torque 1 off
        off off
178
179 #applying normal force in the top of the tip
180 fix fix_forca_normalID top_blockG addforce 0.0 0.0 ${F_normal}
181
182 #distribution of atoms between the processing cores
183 balance 1.1 shift xyz 50 1.0
184
185 #couple the spring in the center of mass of the tip
186 #the spring equilibrium distance is defined as the initial distance
        until the center of mass
187 variable equilibrium_distance equal xcm(blockG,y)
188 print "Tip center of mass in -y= ${equilibrium_distance}"
189 fix  springID top_blockG spring tether 3.0 NULL ${equilibrium_distance}
        NULL 0.0
190
191 thermo_style custom step pe temp f_springID[2] c_comBloco[1] c_comBloco
        [2] c_comBloco[3]
192
193 # ensemble NVT com a temperatura definida no inicio do arquivo
194 fix fixnvtblocoID nvtblocoG nvt temp ${T} ${T} 0.5
195 fix fixnvtslabID nvtslabG nvt temp ${T} ${T} 0.5
196
197 fix fixnveblocoID nveblocoG nve
198 fix fixnveslabID nveslabG nve
199
200 #change the spring variables for the log file
201 variable   spring_fx   equal f_springID[1]
202 variable   spring_fy   equal f_springID[2]
203 variable   spring_fz   equal f_springID[3]
204 variable   spring_ftot  equal  f_springID[4]
205
206 #fix the base of the slab
207 fix setforcefixoID fixoG setforce 0.0 0.0 0.0
208 fix nvefixo fixoG nve
209
```

```
210  ######################################################################
211  #### EXECUTION
212  ######################################################################
213  timestep 0.0001
214
215  #system relaxation
216  run 60000
217
218  #move the inferior slab
219  velocity fixoG set 0.0 1.0 0.0
220
221  run 540000
222  write_restart restart.simulation
```